Ophicarbonate evolution from seafloor to subduction and implications for deep-Earth C cycling

E. Cannao, M. Scambelluri, Gray E. Bebout, S. Agostini, T. Pettke,
Marguerite Godard, L. Crispini

Ophicarbonate evolution from seafloor to subduction and implications for deep-Earth C cycling

E. Cannaò [a], M. Scambelluri [b], G. E. Bebout [c], S. Agostini [d], T. Pettke [e], M. Godard [f], L. Crispini [b]

[a] *Dipartimento di Scienze della Terra "A. Desio", Università di Milano, Via Botticelli 23, 21133 Milano, Italy*

[b] *Dipartimento di Scienze della Terra, dell'Ambiente e della Vita, Università di Genova, C.so Europa 26, 16132 Genova, Italy*

[c] *Department of Earth and Environmental Sciences, Lehigh University, Bethlehem, PA 18015, USA*

[d] *Istituto di Geoscienze e Georisorse, CNR, Via Moruzzi 1, 56124 Pisa, Italy*

[e] *Institute of Geological Sciences, University of Bern, 1+3 Baltzerstrasse, CH-3012, Bern, Switzerland*

[f] *Geosciences Montpellier, CNRS, Universite de Montpellier, Place Eugene Bataillon, 34095 Montpellier, France*

1 **Abstract**

2   The chemical and physical processes operating during subduction-zone metamorphism

3 can profoundly influence the cycling of elements on Earth. Deep-Earth carbon (C) cycling

4 and mobility in subduction zones has been of particular recent interest to the scientific

5 community. Here, we present textural and geochemical data (C-O, Sr isotopes and bulk and

6 *in-situ* trace element concentrations) for a suite of ophicarbonate rocks (carbonate-bearing

7 serpentinites) metamorphosed over a range of peak pressure-temperature (*P-T*) conditions

8 together representing a prograde subduction zone *P-T* path. These rocks, in order of

9 increasing peak *P-T* conditions, are the Internal Liguride ophicarbonates (from the Bracco

10 unit, N. Apennines), pumpellyite- and blueschist-facies ophicarbonates from the Voltri Massif

11 (W. Ligurian Alps) and the Queyras (W. Alps), respectively, and eclogite-facies

12 ophicarbonates from the Voltri Massif. The Bracco oceanic ophicarbonates retain breccia-like

13 textures associated with their seafloor hydrothermal and sedimentary origins. Their trace

14 element concentrations and $\delta^{18}O_{VSMOW}$ (+15.6 to +18.2‰), $\delta^{13}C_{VPDB}$ (+1.1 to +2.5‰) and

15 their $^{87}Sr/^{86}Sr$ (0.7058 to 0.7068), appear to reflect equilibration during Jurassic seawater-rock

16 interactions. Intense shear deformation characterizes the more deeply subducted

17 ophicarbonates, in which prominent calcite recrystallization and carbonation of serpentinite

18 clasts occurred. The isotopic compositions of the pumpellyite-facies ophicarbonates overlap

19 those of their oceanic equivalents whereas the most deformed blueschist-facies sample shows

20 enrichments in radiogenic Sr ($^{87}Sr/^{86}Sr$ = 0.7075) and depletion in ^{13}C (with $\delta^{13}C$ as low as -

21 2.0‰). These differing textural and geochemical features for the two suites reflect interaction

22 with fluids in closed and open systems, respectively. The higher-*P*-metamorphosed

23 ophicarbonates show strong shear textures, with coexisting antigorite and dolomite, carbonate

24 veins crosscutting prograde antigorite foliation and, in some cases, relics of magnesite-

25 nodules enclosed in the foliation. These rocks are characterized by lower $\delta^{18}O$ (+10.3 to

26 13.0‰), enrichment in radiogenic Sr ($^{87}Sr/^{86}Sr$ up to 0.7096) and enrichment in incompatible

27 and fluid-mobile element (FME; e.g., As, Sb, Pb). These data seemingly reflect interaction

28 with externally-derived metamorphic fluids and the infiltrating fluids likely were derived

29 from dehydrating serpentinites with hybrid serpentinite-sediment compositions. The

30 interaction between these two lithologies could have occurred prior to or after dehydration of

31 the serpentinites. We suggest that decarbonation and dissolution/precipitation processes

32 operating in ancient subduction zones, and resulting in the mobilization of C, are best traced

33 by a combination of detailed field and petrographic observations, C, O and Sr isotope

34 systematics (i.e., 3D isotopes), and FME inventories. Demonstration of such processes is key

35 to advancing our understanding of the influence of subduction zone metamorphism on the

36 mobilization of C in subducting reservoirs and the efficiency of delivery of this C to depths

37 beneath volcanic arcs and into the deeper mantle.

38

39 *Keywords: oceanic ophicarbonates; high-pressure ophicarbonates; deep Carbon cycle;*

40 *subduction zone; C-O-Sr isotopes*

41

1. Introduction

43 Ophicarbonates (i.e., carbonated ultramafic rocks) are potentially important carbon (C)

44 reservoirs influencing the long-term C cycle in the solid Earth. Large volumes of

45 ophicarbonate form by peridotite alteration at the seafloor, causing low- to moderate-

46 temperature (*T*) serpentinization (e.g., Mével, 2003; O'Hanley, 1996) and carbonation by

47 mixed seawater and alkaline hydrothermal fluids (e.g., Lost City hydrothermal fields, Früh-

48 Green et al., 2004; Kelley et al., 2005; Ludwig et al., 2006). Ophicarbonates display

49 brecciated textures consisting of serpentinite clasts enclosed by sets of carbonate veins and/or

50 by a micrite matrix. Such rocks occur in present-day oceans (e.g., the Atlantic; Bonatti, 1976)

51 and their abundance in ophiolitic complexes documents ophicarbonate formation also in

52 ancient oceans (e.g., Früh-Green et al., 1990; Schwarzenbach et al., 2013; Tartarotti et al.,

53 2019; Weissert and Bernoulli, 1984). Ophicarbonates can also form at depth in subduction

54 zones via interaction of (meta)serpentinite with carbonic fluids leading to carbonation of rock-

55 forming silicates and to C sequestration into oceanic slabs and supra-subduction mantle

56 (Piccoli et al., 2016; Scambelluri et al., 2016). These two processes together affect C storage

57 and transport from oceans to subduction zones and the transfer of C-O-H fluids into volcanic

58 arcs (Alt et al., 2013; Collins et al., 2015; Kerrick and Connolly, 1998; Scambelluri et al.,

59 2016) or in deeper parts of the mantle.

60   Experiments and thermodynamic modelling suggest relative immobility of C in

61 subducting oceanic crustal rocks to very high pressure-temperatures (*P-T*) conditions unless

62 the rocks are infiltrated by H_2O-rich fluids (Collins et al., 2015; Kerrick and Connolly, 2001,

63 1998; Molina and Poli, 2000; Poli et al., 2009). Studies of exposed high-*P/T* metamorphic

64 rocks document some C mobilization during subduction either by decarbonation reactions or

65 by carbonate dissolution in aqueous fluids (Ague and Nicolescu, 2014; Cook-Kollars et al.,

66 2014; Frezzotti et al., 2011; Malaspina et al., 2009; Piccoli et al., 2016; Sapienza et al., 2009;

67 Scambelluri et al., 2016); however, the scale of this related C transport has remained unclear

68 (see the discussion by Epstein et al. 2019). Field and stable isotope studies of high-*P* and

69 ultrahigh-pressure *(UHP)* metamorphic suites indicate that the extent of C mobilization by

70 these processes is highly dependent upon the degree to which rocks behave as systems open

71 to infiltration by externally-derived H_2O-rich fluids (Collins et al., 2015; Epstein et al., 2019).

72   Serpentinite is pivotal in the subduction zone C cycle because, as the result of antigorite

73 dehydration, it supplies H_2O to adjacent carbonate rocks, thus potentially driving

74 decarbonation reactions (i.e., destabilization of carbonates) and carbonate dissolution.

75 Moreover, serpentine is reactive to C-O-H fluids and sequesters CO_2 from fluids via

76 carbonation of its silicate minerals (Scambelluri et al., 2016). The study of ophicarbonates is

77 timely, given recent interest in subduction zone C cycling, and can address the mechanisms of

C-storage and loss within a single, complex rock system and between serpentinite and carbonate-bearing reservoirs.

Abundant petrographic and petrologic work available to date deals with present-day and fossil oceanic ophicarbonate rocks (Bonatti, 1976; Clerc et al., 2014; Collins et al., 2015; Cortesogno et al., 1980; Driesner, 1993; Galli and Togliatti, 1965; Lafay et al., 2017; Treves et al., 1995; Weissert and Bernoulli, 1984); however, less attention has been paid to ophicarbonate evolution during subduction-zone metamorphism (Collins et al., 2015; Debret et al., 2018; Driesner, 1993; Scambelluri et al., 2016). We focused on ophicarbonates exposed in Alpine-Apennine ophiolite sequences representing a wide range of peak metamorphic *P-T*, from low-*T* oceanic conditions recorded by Apennine ophicarbonates, to pumpellyite-, blueschist- and eclogite-facies conditions experienced by ophicarbonates from the Ligurian and the Western Alps. In this paper, based on study of high-*P* metamorphic rocks, we demonstrate that decarbonation and dissolution/precipitation processes operating in ancient subduction zones are best traced by a combination of detailed field and petrographic observations, FME inventories, and C, O, and Sr isotope systematics (i.e., 3D isotopes).

2. Geological setting

2.1. Northern Ligurian Apennine ophicarbonates

In the Northern Ligurian Apennine, ophiolites either occur as large olistoliths (in the sedimentary flysch of the External Liguride Units) or form large coherent bodies (in the Internal Liguride Units). In the latter setting, ophicarbonates (**Fig. 1A**) occur at the stratigraphic top of the serpentinized mantle (e.g., Cortesogno et al., 1980) and are overlain by pillow basalt and oceanic sediments (i.e., radiolarian cherts, limestone and mudstone). In such a cases, the Moho is commonly represented by preserved primary contacts of serpentinite-ophicarbonate with pillow basalt and, locally, with extensional tectonic breccia and deep

104   oceanic sediments (Alt et al., 2018; Decandia et al., 1998; Lagabrielle, 1987). Thus far,

105   tectonic (OCI) and sedimentary (OCII) ophicarbonates have been distinguished based on

106   textural and petrographic features (e.g., Lemoine et al., 1987). The OCI type is characterized

107   by polyphase brittle-ductile to brittle deformation (Treves and Harper, 1994). These rocks

108   display early serpentine formation after mantle minerals and in shear extensional veins,

109   followed by infiltration of CO_2-rich fluids to form a sequence of generations of calcite veins

110   in response to increasing hydrothermal fluid pressure ($P_{fluid}/P_{lithostatic}$ >1). The last brittle

111   deformation led to formation of veins filled by calcite and talc druses (Treves and Harper,

112   1994). The set of tectonic and hydrothermal structures recorded by the OCI is related to the

113   tectonic exposure of the oceanic mantle at surface levels under progressively lower

114   temperature conditions at extensional core-complexes at slow-spreading ridges. The OCI

115   samples are thus representative of extensional fault settings (Treves and Harper, 1994) and are

116   comparable with ophicarbonates beneath the Lost City hydrothermal vent at the Mid-Atlantic

117   Ridge (e.g., Ludwig et al., 2006). Tectonic-sedimentary reworking of the exposed

118   serpentinized mantle, coupled with calcite precipitation, leads to the formation of OCII

119   showing angular to sub-angular serpentinite clasts of varying sizes embedded in a micrite

120   sedimentary matrix (Treves and Harper, 1994). Oxidation and carbonation processes

121   accompany the hydrothermal alteration, allowing formation of hematite and thus conferring

122   upon these rocks a typical red color during a process thought to have generated the Ligurian

123   ophicarbonate variety know as *Rosso di Levanto* (Galli, 1957).

124

2.2 Western Alps

126   The Alpine architecture consists of large tectonic units of continental and oceanic

127   affinity (e.g., Dal Piaz et al., 2003): the ophicarbonate rocks studied here belong to the

128   oceanic lithosphere exposed at three main localities of the Upper Penninic nappe stack and

129   recording progressively higher peak metamorphic *P-T* during subduction (**Fig. 1**). From lower

130 to higher grade, the sampled localities are: the pumpellyite-actinolite facies Sestri-Voltaggio

131 Zone (Ligurian Alps), the blueschist-facies Queyras (Ubaye locality; French Alps), and the

132 eclogite-facies-metamorphosed Voltri Massif (Ligurian Alps).

133

2.2.1 Sestri-Voltaggio zone

135 The Sestri-Voltaggio zone consists of several tectonic units and is believed to represent

136 the N-S junction zone between the Alpine chain and the Northern Apennines (Crispini and

137 Capponi, 2001). The ophicarbonate rocks sampled in this area belong to the Figogna unit,

138 consisting of oceanic lithospheric mantle comparable to that in the Voltri Massif, but which

139 escaped eclogite facies metamorphism during Alpine subduction. The metamorphic grade of

140 this unit is pumpellyite-actinolite facies, in the stability field of lawsonite (270-320 °C and 0.6

141 GPa; Leoni et al., 1996). Here ophicarbonates crop out near the village of Pietralavezzara in

142 decametric-sized slices with N-S orientations (PL samples in **Fig. 1C**). Despite the polyphase

143 deformation that affected the Figogna unit, the original oceanic sequence showing

144 ophicarbonates on top of the ultramafic and gabbroic basement, and below a volcano-

145 sedimentary cover, can still be recognized (Crispini and Capponi, 2001).

146

2.2.2 Queyras complex

148 The Queyras complex is part of the Piedmont-Ligurian domain, west of the eclogite-

149 facies Monviso ophiolite and near the contact with the Brianconnais domain (**Fig. 1B**). This

150 complex was interpreted as a sedimentary accretionary wedge composed of oceanic sediments

151 and accreted slices of oceanic lithosphere (Lafay et al., 2013; Lagabrielle et al., 1985). The

152 metamorphic grade increases eastwards, from temperature < 350 °C and pressure < 1.1 GPa,

153 to *P-T* conditions pertaining to the blueschist-facies conditions (up to 480 °C and P > 1.2

154 GPa; Agard et al., 2001). The Queyras ophiolite crops out as scattered large olistoliths within

155 the metasedimentary Schistes Lustrés: the ophiolite bodies preserve the original internal

156 structure and stratigraphy, enabling reconstruction of their oceanic history (Tricart and

157 Lemoine, 1991). Within each body, three major components of the oceanic lithosphere can be

158 distinguished; from bottom to top these are (i) an ultramafic sequence of serpentinized

159 mantle-derived peridotites, locally crosscut by Late Triassic gabbro intrusions (Carpena and

160 Caby, 1984), (ii) a discontinuous basaltic layer of tholeiitic pillow basalts, and (iii) a

161 sedimentary pelagic cover represented by the Schists Lustrés complex. Where the basaltic

162 sequence is missing, the ultramafic and the sedimentary rocks can be directly in contact

163 (Tricart and Lemoine, 1991). The ophicarbonate rocks are on top of the ultramafic sequence

164 and can be subdivided into groups of tectonic (OCI) and sedimentary (OCII) origin. The first

165 type is characterized by a dense network of calcite veins and fractures formed by tectonic

166 extension and hydraulic fracturing; the OCII type derives from in-situ reworking of OCI, of

167 serpentinites and/or basaltic materials forming clasts in a micrite matrix (e.g., Lemoine et al.,

168 1987). The presence of ophicarbonate rocks is interpreted as representing exposure of mantle

169 to seawater on the ocean floor (Tricart and Lemoine, 1991). The ophicarbonate samples

170 analyzed in this study (CU samples in **Fig. 1B**) experienced blueschist-facies *P-T* conditions

171 (325 – 375 °C and 1.1 – 1.4 GPa; Michard et al., 2004).

172

2.2.3 Voltri Massif

174 The ophiolitic Voltri Massif is a blueschist- to eclogite-facies complex of Jurassic

175 oceanic lithosphere composed of serpentinites hosting gabbro- and basalt-derived eclogite and

176 metarodingite. This sequence is associated with high-*P*-metamorphosed oceanic sediment, i.e.

177 calc- and mica-schists (referred to as Schistes Lustrés) interlayered with metabasalts and

178 cherts (e.g., Chiesa et al., 1975). Remnants of sub-continental lithospheric mantle are well-

179 exposed in the Erro-Tobbio metaperidotite unit, representing the pre-Alpine rifting and ocean-

180 floor alteration followed by subduction and metamorphism at eclogite-facies *P-T* conditions

181 (Hermann et al., 2000; Hoogerduijn Strating et al., 1993; Scambelluri et al., 1995, 1991;

182 Vissers et al., 1995, 1991). Peak metamorphic *P-T* estimates for the Voltri Massif are about

183 450 – 500 °C and 1.3 – 1.7 GPa (Cimmino et al., 1979; Federico et al., 2004; Messiga and

184 Scambelluri, 1991), conditions that produced metamorphic olivine + antigorite in

185 serpentinites, garnet + omphacite + rutile in eclogite and high-Si-bearing phengite + garnet in

186 metasedimentary rocks. Field and geochemical evidence (Cannaò et al., 2016; Federico et al.,

187 2007; Scambelluri and Tonarini, 2012), together with numerical modelling (Malatesta et al.,

188 2012), suggests a complex history for the Voltri Massif during prograde and retrograde

189 evolution along the slab-mantle interface.

190 　　The ophicarbonate rocks of the Voltri Massif crop out in several localities (**Fig. 1**) and

191 were first described by Cortesogno et al. (1981, 1980). These rocks consist of carbonate

192 mineral phases (calcite, dolomite and/or magnesite) coexisting with antigorite and, locally,

193 metamorphic olivine. These rocks are interpreted as the metamorphic counterparts in the non-

194 subducted oceanic ophicarbonates of the Northern Apennines ophiolites, with grades ranging

195 from greenschist-, to blueschist-, to eclogite-facies. Recently, Scambelluri et al. (2016)

196 described in detail the evolution, metamorphic reactions, and C and O isotope compositions at

197 an outcrop within the Voltri Massif, highlighting the high potential of serpentinite for

198 sequestering C and thus influencing the deep C cycle. The samples from the Voltri Massif

199 analyzed in this study are from two localities representing ophicarbonates affected by the

200 eclogite-facies metamorphism: La Pesca (Scambelluri et al., 2016; LP13 EOC samples) and

201 Sant'Anna (SA samples).

202

3. Petrography and microstructures

204 　　The ophicarbonate samples presented here retain evidence of complex polyphase

205 histories. Here, we describe the key features of representative ophicarbonate samples from

206 each locality: for the Northern Apennine, we retain the classification of the ophicarbonates of

207 tectonic-hydrothermal (OCI) and sedimentary (OCII) origin initially proposed by Lemoine et

208 al. (1987). Also, we describe the oceanic serpentinite exposed in the Northern Apennine,

209 regarding it as the starting material (protoliths) for the higher-grade ophicarbonates.

210

3.1 Oceanic Northern Apennine Ophicarbonates

Serpentinite protolith rocks

213   The ultramafic protoliths of the oceanic ophicarbonates are represented by highly (90%)

214 to fully (100%) serpentinized mantle peridotites. In these rocks, static pseudomorphic

215 replacement led to formation of mesh serpentine + magnetite textures after mantle olivine and

216 bastite after mantle pyroxenes in which traces of the former pyroxene cleavage are still

217 recognizable. The medium grain size of the pseudomorphs and the isotropic texture suggest

218 an original harzburgite for these ultramafic rocks. The sample collected in this study does not

219 display evidence for deformation, but high-*T* shear domains are described in the literature for

220 the serpentinite basement (Treves and Harper, 1994).

221

Ophicarbonates of tectonic and hydrothermal origin (OCI)

223   The ophicarbonates of tectonic and hydrothermal origin (OCI) contain several

224 generations of carbonate veins overprinting the serpentinized precursor. Calcium carbonate is

225 the most widespread mineral, ubiquitous in these rocks at this stage. Samples can display

226 variably extensive carbonation of the starting serpentinite during the hydrothermal activity.

227 The amounts of vein-related calcite can range from few modal % calcite (e.g., ZRL 15-3) to

228 more than 80 % (e.g., MNT 13-5) of the host rock. The host serpentinite has the texture of a

229 jigsaw puzzle breccia with clasts ranging in size from the outcrop scale (m in size) to hand-

230 sample size (few cm)- and to mm-scale. The ultramafic clasts also display varying extents of

231 carbonation, from less than 20% (ISC 13-1) to 90% (ZRL 13-1) in volume.

232   The ultramafic clasts correspond to fully serpentinized peridotites, which do not

233 preserve olivine and which rarely preserve relict mantle pyroxene and spinel partially

234 converted to magnetite. The clasts of the host serpentinite are heterogeneous in size and

235 polygonal in shape, with sub-angular to angular edges. Each clasts preserves a record of the

236 original undeformed and deformed structure of the serpentinized mantle peridotite host. The

237 monotonous chrysotile + magnetite assemblage of the pure serpentinite clasts is locally

238 accompanied by formation of chlorite, talc and tremolite. Near the calcite hydrothermal veins,

239 the serpentinite clasts unaffected by carbonation and preserving mantle pyroxene relics show

240 evidence of infiltration in the form of small- to medium- sized calcite veinlets.

241 The serpentinite clasts are affected by varying degrees of carbonation: from minor

242 overgrowth by neoblastic fine-grained calcite to reddish clasts showing pervasive to full

243 carbonation associated with oxidation. This carbonation represent a key feature of such

244 hydrothermally-altered oceanic ophicarbonates: full carbonation of the ultramafic silicate

245 clasts concurs with formation of variably abundant hematite after magnetite. Replacement by

246 calcite of serpentine from the core of the mesh texture and along cleavage of the former

247 pyroxene by calcite occurs in nearly all oceanic samples. Locally, along the cleavages of

248 serpentinized pyroxenes, trails of small green andraditic garnet crystals are intergrown with

249 serpentine and calcite (**Fig. 2C**). In samples where the carbonation has been quite extensive,

250 the serpentinite clasts are entirely replaced by fine-scale calcite grains and a film of hematite

251 grows along the border, giving them a ghost-like texture (**Fig. 2A, B**). Interestingly, the full

252 carbonation of the ultramafic silicate clasts appears to be associated with the formation of

253 abundant hematite (**Fig. 2A, B**), suggesting that the Fe^{2+} released by the carbonated silicates

254 was converted to Fe^{3+} thus stabilizing hematite due to increased oxidizing conditions.

255 The last brittle deformation event recorded by these rocks is represented by the

256 formation of calcite veins that crosscut all previous structures. Calcite is coarse-grained and

257 shows euhedral habit and, typically, twinning. Talc is observed in drusy textures commonly in

258 the core of the veins, seemingly representing as the last precipitates. In some samples, calcite

259 is replaced by talc aggregates (**Fig. 2D**).

Sedimentary ophicarbonates (OCII)

These rocks display a sedimentary breccia-like texture with clasts consisting of serpentinites or of reworked OCI. The sedimentary OCII clasts typically display angular edges and widely varying grain size from several millimeters to few hundreds of micrometers. The mineral assemblage of the clasts, as in the OCI, consists of serpentine, magnetite, chlorite, talc and minor tremolite. Based on the extent of carbonation and oxidation, two types of sedimentary breccias can be identified: (i) samples SG 15-4 and MNT 15-2, showing minor and abundant carbonation and oxidation, respectively, and (ii) sample SG 15-2, showing intermediate amounts of carbonation and oxidation.

The green colour of ophicarbonate SG 15-4 reflects the high modal abundance of hydrous silicate minerals still preserved in the rock. The textures of the serpentinite clasts preserve the mantle mineral domains; however, some clasts with complex texture likely derive from pre-existing serpentine veins. The matrix calcite range from micritic to sparry, the latter occurrence type showing twinning. The sedimentary structures are cut by calcite veins showing, from rim to core, a change from botryoidal to irregular blocky textures (**Fig. 2E**).

The ophicarbonate sample MNT 15-2 shows an intense degree of carbonation and oxidation, with a reddish color due a large amount of hematite (**Fig. 2F**). In sample SG 15-2, only a few % of the clasts still preserve the original serpentinite composition, while widespread ghost-like textures derive from full replacement of former silicate minerals by fine-grained calcite. Locally, the clasts are composed of single crystals of calcite, probably derived from reworking of the OCI and associated hydrothermal calcite veins. The matrix of sample MNT 15-2 consists mainly of medium- to fine-scale (to microcrystalline) grains of anehdral calcite with lobate and irregular intercrystalline boundaries. Along the contact between the clasts and the matrix, calcite grows as cement crusts typically forming gravitational beard-like patterns.

3.2 Subduction-related ophicarbonates

Pumpellyite-actinolite-facies ophicarbonates

Samples PL 13-1 and PL 13-2 display two texturally different types of micro-domains indicating multiple stages of recrystallization of calcite grains. The first micro-domain consists of coarse- to medium-sized grains of calcite (1) showing development of a second generation of twin lamellae cutting at high angles the earlier-formed generation and affected by growth of twin-free calcite grains. The coarse calcite (1) is cut by shear zones that represent the second type of micro-domain observed in these samples. The shear zones consist of medium- to fine- grained, un-twinned calcite (2) irregular in shape and with complex grain boundaries. Along the shear zones, calcite (1) is partially recrystallized and becomes elongated and re-oriented coherently into the shear zone orientation (**Fig. 3A**). Both samples (PL 13-1 and PL 13-2) also contain 10-20 volume % serpentinite clasts ranging in size from several centimetres to a few millimetres. In general, the largest clasts are broken into smaller pieces when embedded and displaced along the shear-zones as sigmoidal porphyroclasts. The serpentine clasts consist of magnetite and antigorite showing tabular and interlocking textures grown at the expense of mesh-like lizardite/chrysotile. In shear zones, thin dark films of antigorite are interlayered with the calcite (2), giving to the rock an S-C like texture. The serpentinite clasts in these samples thus derive from an early stage of oceanic serpentinization and carbonation.

A key feature pertaining to these samples is the replacement of antigorite within the clasts by neoblastic calcite. Calcite overgrowths occur along the contacts between antigorite and calcite within the shear zones and inside the various serpentine clasts (**Fig. 3B**). These textures indicate that replacement of serpentine by calcite was due to syn-deformation infiltration by carbonic fluids.

Blueschist-facies ophicarbonates

313   Samples CU3 and CU 13-1 represent ophicarbonates re-equilibrated at blueschist-facies

314   *P-T* conditions. CU3 consists of coarse serpentinite clasts in a coarse-grained calcite matrix.

315   In the clasts, antigorite overgrows earlier serpentine minerals and, in the majority of the clasts,

316   the original serpentinite texture is cross-cut and overgrown by networks of calcite-bearing

317   veins. The coarse-grained matrix-forming calcite is anhedral and shows corroded grain

318   boundaries, undulose extinction, and abrupt change in the twin growth, features that together

319   represent deformation during crystallization. The calcite grains formed along the contacts

320   with the serpentinite clasts and within the fracture network (**Fig. 3C**) display elongate textures

321   suggesting syn-deformation crystallization.

322   Sample CU 13-1 shows the development of carbonate-rich shear zones alternating with

323   domains with abundant serpentinite clasts. The shear zone textures are quite similar to those

324   in samples PL 13-1 and PL 13-2 and are characterized by re-orientation of calcite and

325   serpentinite clasts along the shear foliation and by crystallization of neoblastic calcite

326   emanating from the grain boundaries of former calcite (**Fig. 3D**). Deformation within the

327   shear zones leads to fracturing of the serpentinite clasts, grain size reduction, and uniform

328   orientation of the antigorite flakes. Within the shear zones, the matrix calcite is very fine-

329   grained (maximum 100 μm) and shows heterogranular and hypidiotopic fabric typical of

330   dynamic recrystallization and imparting a marble-like texture. The lack of twin lamellae in

331   this type of calcite suggests an increase in the *T* conditions with respect to that experienced by

332   the coarse-grained calcite crystals.

333

Eclogite-facies ophicarbonates

335   Samples from the La Pesca locality (LP13 EOC1 and LP13 EOC3) display an antigorite

336   + calcite + magnetite (± hydro-garnet in sample LP13 EOC1) mineral assemblage. As in the

337   oceanic samples, garnet forms along the cleavages of the serpentinized pyroxene and, locally,

338 around magnetite pods displaced along the main foliation (**Fig. 3E**). As often occurs in

339 serpentinite, the magnetite pods may derive from oceanic alteration and recrystallization of

340 Cr-rich mantle spinel. The main difference between the two La Pesca samples is the strong

341 deformation affecting LP13 EOC3, a texture similar to that of samples CU 13-1 and PL 13-

342 1/2. Despite the textural similarity to CU 13-1 and PL 13-1/2, deformed calcite in sample

343 LP13 EOC3 is much finer-grained and contains more equigranular fabrics and hypidiotopic to

344 idiotopic crystals. Sample LP13 EOC1 largely consists of calcite veins cutting the entire rock

345 structure and suggesting late (subduction-related?) infiltration of C-bearing fluids along

346 fractures.

347 The S. Anna ophicarbonates are the only samples showing dolomite and magnesite

348 associated with antigorite, magnetite, minor chlorite, and diopside. In these rocks, coarse

349 porphyroclastic magnesite occurs within the foliation produced at high-*P* conditions, probably

350 as the result of tectonic dismemberment of former veins (sample SA 15-8). An interesting

351 feature of this magnesite is the presence of primary and pseudo-secondary fluid inclusions

352 (**Figs. 3G, 3H**) showing tabular shapes, variable size (from 20 to few μm) and infilling by

353 liquid + gas. Occasionally, small aggregates of Ti-clinohumite are present and associated with

354 the magnesite grains. Magnesite is partially replaced by dolomite and calcite along contacts

355 with antigorite and, concurrent with this replacement, acicular tremolite was formed after

356 antigorite.

357 Sample SA 15-1 shows micro-scale shear zones similar to those found in the other

358 subduction-related samples: in such sheared domains, dolomite is overgrown by calcite,

359 antigorite and minor chlorite likely related to retrograde deformation. Though high-*P*

360 conditions were reached in the S. Anna area, as described in literature, no evidence of

361 metamorphic olivine has been found in the samples investigated here. However, we interpret

362 the dolomite + antigorite + diopside assemblage (**Fig. 3F**) as representing high-*P* conditions

363   comparable with those of the ophicarbonates from the Zermatt-Saas Unit (Chatillon area, W.

364   Alps), the latter peak-metamorphosed at 1.4 GPa and 450-550 °C (Driesner, 1993).

365

366   **4. Methods**

367   *4.1 Bulk rocks*

368   Whole rock major element analyses were performed at ActLabs Ltd. using a fusion

369   technique employing a Li-metaborate/tetraborate fusion digested in a weak nitric acid and

370   measured by ICP-OES. Accuracy and precision are estimated as better than 1%. Loss on

371   ignition (LOI) was determined by weight difference following ignition of samples in a

372   furnace. The amount of CO_2 was determined by calcimetry at the IGG-CNR (Pisa, Italy) by

373   reacting small aliquot of sample (about 0.3 g) with HCl, and measuring the release of CO_2

374   from carbonates through the volume of water shifted in a graduated cylinder. The

375   concentration is then calculated using a calibration line. The CO_2 measured from sample

376   containing the less-reactive magnesite in the assemblage (i.e., SA 15-8) may be

377   underestimated. The amount of H_2O was estimated by the simple difference between LOI and

378   CO_2 contents for each sample.

379   Trace element concentrations (except for B) were accomplished using an Agilent 7700x

380   quadrupole ICP-MS at Géosciences Montpellier (AETE-ISO facility, Montpellier, France)

381   following the procedure described in Godard et al. (2000) and Ionov et al. (1992). Boron

382   concentrations for all samples were determined by isotope dilution using the NIST SRM 982

383   spike in a single collector VG Isomass 54E positive thermal ionization mass spectrometer (P-

384   TIMS) running in dynamic mode at the IGG-CNR (Pisa, Italy).

385

386   *4.2 Mineral compositions*

387   Major element mineral compositions were measured at the Department of Earth

388   Sciences, University of Milano (Italy), using the electron microprobe JEOL Superprobe 8200.

389   The analyses were conducted with a WDS system at 15.0 kV, 5 nA for the electron beam and

390   1 μm beam size. We used natural silicate standards (the numbers refer to the international

391   standards): Mg on olivine 153, Fe on fayalite 143, Na on omphacite 154, Ti on ilmenite, Mn

392   on rodonite, K on k-feldspar 113, Al and Ca on anorthite 137, Cr on metallic/pure Cr and Si

393   on wollastonite.

394   Mineral trace element concentrations were determined at the University of Bern by laser

395   ablation, using a Geolas Pro 2006 193 nm ArF excimer laser coupled to an Elan DRC-e ICP-

396   MS instrument (LA-ICP-MS). Analytical strategies, data reduction and instrument

397   optimization procedures closely follow those reported by Spandler et al. (2011) and Pettke et

398   al. (2012). Beam sizes were as large as possible (up to 160 μm diameter) to lower the

399   detection limits, calculated using the stringent formulation in Pettke et al. (2012). External

400   standardization was against the GSD-1D basalt glass, employing the values cited in Peters

401   and Pettke (2017) and the GeoRem data base (Jochum et al., 2005). Data reduction employed

402   SILLS (Guillong et al., 2008), and the sum of all measured element oxides (total oxides, i.e.,

403   100 wt.% minus LOI; e.g., Halter et al., 2002) was used as the internal standard for

404   quantification. Due to the lack of data for Fe^{3+}/Fe^{2+}, total Fe was calculated as FeO. Ablation

405   rates were turned to c. 0.08 μm per pulse via attenuation of the laser output beam; the laser

406   repetition rate was 10 Hz. Measurement accuracy and precision were monitored by analysing

407   SRM612 glass from NIST as an unknown, and the data mostly agree to within 5% of the

408   reference values (**Supplementary Table A3**).

409

410   *4.3 Isotopic analyses*

411   The samples were analyzed for $\delta^{13}C$ and $\delta^{18}O$ at the Department of Earth and

412   Environmental Sciences, Lehigh University (USA), using a Finnigan MAT 252 gas mass-

413   spectrometer coupled with a GasBench II system, applying the methods described by Cook-

414   Kollars et al. (2014) and Collins et al. (2015). We analyzed bulk rocks as well as more pure

carbonates from different textural settings sampled by micro-drilling, using tungsten carbide

bits with diameter of 1 and 2 mm. Calcite, dolomite or magnesite was reacted at 72 °C for 30

min, 3 or 6 hours, respectively, with 0.2 mL 100% phosphoric acid (H_3PO_4) in order to

release CO_2, according to the methods of McCrea (1950), Paul and Skrzypek (2007), and

Sharma et al. (2002). All data are presented in standard delta(δ)-notation, reported relative to

VPDB and VSMOW for $\delta^{13}C$ and $\delta^{18}O$, respectively. Regular analyses of an in-house

standard and the international standard NBS-19 allowed monitoring and correction of the data,

resulting in a standard deviation (1σ) of ~ 0.2‰ for both $\delta^{13}C$ and $\delta^{18}O$.

Strontium isotope analyses were performed using a Finnigan MAT 262 multicollector

mass-spectrometer (at the IGG-CNR, Pisa, Italy), operated in dynamic mode, after ion-

exchange purification through Sr-spec resin. Measured $^{87}Sr/^{86}Sr$ ratios were normalized to

$^{86}Sr/^{88}Sr = 0.1194$. Replicate analyses of NIST SRM 987 ($SrCO_3$) standard gave an average

value of 0.710207 ± 13 (2SD, n = 5). Published values are adjusted to $^{87}Sr/^{86}Sr = 0.710250$.

Strontium blanks were about 0.3 ng, which are negligible given the Sr concentrations in the

samples analyzed in this study.

5. Results

5.1 Bulk rock major and trace element concentrations

The major element whole-rock concentrations of the samples are reported in **Table 1**.

The compositions of ophicarbonates are linked to the proportion of ultramafic and carbonate

component present: here, the composition of a pure serpentinite and an oceanic limestone

(MNT 15-1 and ZRL 15-7, respectively) were considered as the end-members for all of the

ophicarbonate rocks that were investigated. The major element compositions of OCI and

OCII ophicarbonates plot along a linear array in a CaO, MgO and SiO_2 diagram, as do the

subduction-related ophicarbonates. Similar variations in CO_2 and H_2O with respect to MgO

and CaO are displayed for all ophicarbonates, with rocks showing more evidence of

441 recrystallization during subduction processes (e.g. PL 13-2, CU 13-1 and LP13 EOC3)

442 plotting near the CO_2-rich end-member (**Fig. 4**). Sample SA 15-8, which contains magnesite,

443 has a slightly higher MgO concentration and a lower CaO concentrations than the other

444 subduction-related ophicarbonates (**Fig. 4**).

445 Trace element whole-rock compositions of the samples are reported in **Table 1** and in

446 **Fig. 5**. The pure serpentinite sample MNT 15-1 shows low REE concentrations with respect

447 to primitive mantle values (PM, McDonough and Sun, 1995) and a negligible negative Eu

448 anomaly. The strong light (L)REE depletion relative to concentrations of medium (M)REE

449 and heavy (H)REE ($La_N/Nd_N = 0.15$; $Sm_N/Ho_N = 0.36$; $Er_N/Lu_N = 0.81$) suggests a depleted

450 harzburgite protolith. The limestone sample ZRL 15-7 is enriched in LREE to MREE whereas

451 the HREE are almost flat ($La_N/Nd_N = 2.63$; $Sm_N/Ho_N = 2.07$; $Er_N/Lu_N = 1.19$). This sample

452 shows a negative Eu anomaly (($Eu/Eu^*)_N = 0.85$).

453 OCI rocks have complex REE patterns, showing varying degrees of enrichment in

454 LREE ($La_N/Nd_N = 1.76 - 3.80$) and relative depletion in MREE and HREE but with similar

455 Sm_N/Ho_N and Er_N/Lu_N ratios (0.35 and 0.82, respectively) compared to pure serpentinite

456 sample. Only sample ISC 13-1 shows a higher concentration of MREE ($Sm_N/Ho_N = 0.89$). Of

457 the OCI samples, ZRL 13-1 is the only rock with a positive Eu anomaly. The REE patterns of

458 the sedimentary ophicarbonates (OCII) are comparable to those of the OCI rocks, with the

459 exception of sample SG 15-2 that is far more enriched in all REE ($La_N/Nd_N = 1.78$; Sm_N/Ho_N

460 $= 0.89$; $Er_N/Lu_N = 0.93$), although the concentrations are all below those of primitive mantle

461 to which they are normalized. All ophicarbonates have negative Ce anomalies, with $(Ce/Ce^*)_N$

462 ranging from 0.12 to 0.80.

463 Pumpellyite-actinolite-facies ophicarbonates (PL 13-1 and 2) are homogeneous in their

464 abundances of REE with concentrations far lower than those of the primitive mantle. Overall,

465 their REE concentrations differ greatly from those of the oceanic ophicarbonates. More

466 specifically, they show enrichment in LREE ($La_N/Nd_N = 2.77$) without negative Ce anomalies,

467 relatively flat MREE and HREE patterns ($Sm_N/Ho_N = 1.09$; $Er_N/Lu_N = 0.89$), and positive Eu

468 anomalies (($Eu/Eu^*)_N = 1.81$).

469   Blueschist-facies ophicarbonates CU3 and CU 13-1 have similar REE patterns,

470 differing only in their HREE concentrations, the latter lower in sample CU 13-1 ($Er_N/Lu_N = $

471 2.50 against 1.05). They display a slight enrichment in LREE ($La_N/Nd_N = 0.74 - 0.48$), slight

472 depletion in MREE ($Sm_N/Ho_N = 1.25 - 1.35$) and positive Eu anomalies (($Eu/Eu^*)_N = 1.46 - $

473 1.51). For these samples, all PM-normalized REE concentrations fall between 0.1 and 1.

474   The eclogite-facies ophicarbonate LP13 EOC1 shows LREE enrichment ($La_N/Nd_N = $

475 2.24) with a strong negative Ce anomaly, and enrichment of MREE relative to HREE

476 ($Sm_N/Lu_N = 0.54$). Europium shows a slight negative anomaly. Sample LP13 EOC3 shows a

477 similar REE pattern ($La_N/Nd_N = 1.18$ and $Sm_N/Lu_N = 0.62$), but about 1 order of magnitude

478 lower on the normalized plot. The negative Ce anomaly is less pronounced and Eu shows a

479 slight positive anomaly. The eclogite-facies sample SA 15-1, from the S. Anna locality in the

480 Voltri Massif, displays a low La_N/Nd_N ratio (0.70) and shows MREE enrichment relative to

481 HREE ($Sm_N/Lu_N = 3.64$). The magnesite-bearing ophicarbonate (SA 15-8) shows enriched

482 REE concentrations, relative to primitive mantle values, with LREE lower than MREE and

483 HREE ($La_N/Lu_N = 0.33$) and almost flat HREE ($Er_N/Lu_N = 0.92$). Both SA 15-1 and SA 15-8

484 show negative Eu anomalies.

485   The primitive mantle-normalized (PM, McDonough and Sun, 1995) trace elements

486 concentrations of the serpentinite end-member (**Fig. 5C**) are similar to those of seafloor

487 serpentinites imparted by interaction with seawater-derived fluids. These similarities include

488 enrichment in B in (up to 100 times PM) and positive anomalies in Li, Pb, As, Sb and Sr, but

489 always at concentrations lower than those of the primitive mantle. Cesium and Rb

490 concentrations are below detection limits and Ba, U and Th concentrations also are very low.

491   Carbonation processes lead to varying degrees of enrichment in LILE and fluid-mobile

492 elements (FME; e.g., As, Sb, U, Sr and Li) in the oceanic ophicarbonates OCI and OCII (**Fig.**

493 **5C**). Similarity in the extents of enrichment in LILE, B, U, Th, Pb and Li is common for the

494 subduction-related ophicarbonates (**Fig. 5D**). The trace element compositions of the eclogitic

495 samples are comparable to those of the other subduction-related ophicarbonates, with the

496 main differences being their higher Pb, As and Sb concentrations. Niobium and Ta

497 concentrations in sample SA 15-8 are near primitive mantle values whereas the concentrations

498 of these elements in all other samples are very low (between 0.002 and 0.1 normalized to PM

499 values).

500

501 *5.2 Mineral chemistry and in situ trace element concentrations*

502 Major element compositions of representative analyses of minerals in each sample are

503 reported in the **Table 2** and **3** and in the **Supplementary Table S1** and a detailed description

504 of the chemistry of the rock-forming minerals is reported in the **Supplementary Material 1**.

505 Briefly, the serpentine from oceanic and subduction-related ophicarbonates shows major

506 element composition similar to that of serpentine in the pure serpentinite sample characterized

507 by high MgO and SiO_2 contents and varying amounts of TiO_2, Al_2O_3 and Cr_2O_3 related to the

508 mantle mineral that was replaced (i.e., olivine or pyroxenes). Calcium-carbonate ($CaCO_3$) is

509 the dominant component of the carbonates in all oceanic and subduction-related

510 ophicarbonates (> 96%), except in eclogitic samples SA 15-8 and SA 15-1. The latter two

511 samples contain magnesite ($MgCO_3$ > 82% and $FeCO_3$ < 18%) and dolomite (with a Ca/Mg

512 ratio near 1.2) as the most abundant carbonate minerals.

513 The *in-situ* trace element compositions of serpentines and carbonates from the studied

514 samples are reported in **Table 2**, **Table 3**, and in **Figure 6**. When normalized to the primitive

515 mantle values (**Fig. 6A**), the trace element patterns of serpentine minerals from oceanic

516 ophicarbonates show positive anomalies in Cs, U, B, As, Sb, Sr and Li, whereas other LILEs

517 and Th are depleted. Negative HFSE (High Field Strength Elements) anomalies also are

518 present. Compared to the trace element concentrations of the pure oceanic serpentines (grey

519 field in **Fig. 6A**), these serpentinites also are enriched in La with respect to Ce, compatible

520 with the bulk-rock data for OCI and OCII. As expected, calcite in the OCI and OCII samples

521 (**Fig. 6C**) mostly shows enrichment in Sr with scattered enrichments in Rb, Ba, B, La and Li.

522 Calcite from the less carbonated and less oxidized sample SG 15-4 has much higher U

523 concentrations than the calcite in the other samples. As for the serpentine minerals, La in

524 calcite is enriched relative to Ce (e.g., sample MNT 15-2, **Fig. 6C**).

525 Antigorite from subducted ophicarbonates (**Fig. 6B**) shows trace element concentrations

526 comparable to those of the oceanic samples, except for variable Sr anomalies, with the

527 concentrations in general lower than PM in the eclogitic samples and higher than PM in the

528 all other rocks. Notably, As and Sb concentrations in the SA 15-1 and SA 15-8 samples fall at

529 the upper limit of the oceanic field. In situ trace element analyses of the calcites in sample PL

530 13-2 revealed concentrations comparable to those of oceanic OCI (**Fig. 6D**). In contrast, the

531 calcites in the blueschist-facies ophicarbonates are depleted in Li and enriched in Pb and

532 MREE, relative to HREE, and show positive Eu anomalies (**Fig. 6D**) compared with calcite

533 from the oceanic ophicarbonates. Carbonates in the eclogitic samples from La Pesca show

534 trace element patterns comparable to those of oceanic ophicarbonates; however, they show

535 enrichment in W and Pb. Dolomite and calcite in sample SA 15-1 (S. Anna area) are

536 characterized by strong enrichment in LREE, Pb, Sr and MREE relative to HREE. Overall,

537 the concentrations of nearly all trace elements in calcite in this sample are one order of

538 magnitude higher than those in the dolomites. Magnesite in sample SA 15-8 show low

539 concentrations in all trace elements, with very low Sr contents, but with strong enrichment in

540 HREE relative to MREE and LREE.

541

542 *5.3 Isotope geochemistry*

543 *5.3.1 Carbon and oxygen isotope compositions of carbonates*

544 Whole-rock C and O isotope compositions of the carbonate in the ophicarbonate suite

545 analyzed here are listed in **Table 4**. The complete C and O isotope dataset for the micro-

546 drilled carbonates from each of the localities, itemized for texture and mineralogy, is provided

547 in the **Supplementary Table S2** and the Figure in **Appendix A1**.

548 The $\delta^{13}C$ of the oceanic carbonates ranges from about 0.0 to +3.0‰ (**Fig. 7A**), without

549 any significant difference between calcite replacing silicates or calcite in the veins (see the

550 Figure in **Appendix A1**). These results are compatible with previously published data for the

551 Bracco ophicarbonates (Collins et al., 2015; Schwarzenbach et al., 2013). Carbonate in veins

552 has $\delta^{18}O$ values ranging from +18.2 to +26.0‰, whereas values for carbonates within the

553 serpentinite clasts and from the matrix in sedimentary rocks are lower, forming a cluster of

554 +14.3 to 18.9‰ (**Fig. 7A**). The higher $\delta^{18}O$ values correspond to calcite from late-stage veins

555 (**Fig. 2D**).

556 Pumpellyite-facies ophicarbonates (**Fig. 7B**) show $\delta^{13}C$ within the range of the

557 Apennine ophicarbonates (from 0.0 to +1.5‰) and the $\delta^{18}O$ values form a tight cluster

558 ranging from +14.4 to +15.5‰. The blueschist-facies CU3 samples show similar $\delta^{13}C$ (+0.1

559 to +0.9‰) and $\delta^{18}O$ from +15.8 and +17.9‰, but sample CU13-1 has negative $\delta^{13}C$ value (-

560 2.7 to -1.1‰) and $\delta^{18}O$ ranging from +16.4 to +18.1‰. The range shown by the latter sample

561 is compatible with values obtained by Collins et al. (2015) for ophicarbonates and carbonated

562 metabasaltic rocks from the same area (**Fig. 7B**). Eclogitic sample LP13 EOC3 has $\delta^{13}C$

563 ranging from +0.7 to +1.4‰ and $\delta^{18}O$ from 14.1 to 15.7‰, whereas LP13 EOC1 shows

564 similar $\delta^{13}C$ (+0.8 to +1.6‰) but lower $\delta^{18}O$ ranging from +10.8 and +11.5‰ (**Fig. 7B**).

565 Other Voltri Massif ophicarbonates from the S. Anna locality are similar in their $\delta^{13}C$ (+0.4 to

566 +1.7‰) but slightly higher in their $\delta^{18}O$ (+11.6 to +12.7‰, **Fig. 7B**).

567

568 *5.3.2 Strontium isotope compositions*

569   Strontium isotope compositions were analyzed for whole-rocks (except for sample SA

570   15-1) and are listed in **Table 4** and are plotted in **Fig. 8**, against $\delta^{18}O$ and $\delta^{13}C$. The $^{87}Sr/^{86}Sr$

571   data for the Northern Apennines samples are reported for an initial time of 160 Ma, whereas

572   the measured $^{87}Sr/^{86}Sr$ ratio is reported for the subducted ophicarbonates. This choice is based

573   on the fact that the extent of the Sr isotopic re-equilibration during subduction evolution is

574   uncertain. However, as reported in **Table 4**, the differences between measured values and

575   age-corrected Sr isotope compositions for the subducted-related samples (for the Voltri

576   Massif of 33 Ma, Rubatto and Scambelluri, 2003) is very small (within the analytical error)

577   due to the very low Rb/Sr of the samples.

578   The $^{87}Sr/^{86}Sr$ of the pure serpentinite end-member is 0.706929, which is compatible

579   with values for serpentinite formed at the oceanic floor during interaction with seawater at

580   Jurassic time (Jurassic seawater value = 0.7070; Jones et al., 1994). The limestone is

581   characterized by higher Sr isotope value of 0.707048 which is compatible with a re-

582   equilibration with Upper Crataceous seawater (Jones et al., 1994) as proposed by Barbieri et

583   al. (1979). Ophicarbonates of tectonic and sedimentary oceanic origins show $^{87}Sr/^{86}Sr$ ratios

584   similar to those of the pure serpentinite, ranging from 0.705746 to 0.706703. This range

585   confirms the Jurassic oceanic imprint of the ophicarbonates due to interaction between

586   seawater-derived fluids in hydrothermal systems. The pumpellyite- and blueschist-facies

587   ophicarbonates from Pietralavezzara and Ubaye show similar values ranging from 0.706383

588   to 0.706833. The only exception is for sample CU1 13-1 that displays a slight enrichment in

589   radiogenic Sr up to a value of 0.707530, well above the values for Jurassic and Cretaceous

590   seawater. The $^{87}Sr/^{86}Sr$ of sample LP13 EOC3 (0.706791) is comparable to that of oceanic

591   rocks, whereas the other eclogitic ophicarbonates have far more radiogenic compositions:

592   sample LP13 EOC1 and SA 15-8 have $^{87}Sr/^{86}Sr$ = 0.708453 and 0.709670, respectively, and

593   calcite and dolomite separates from sample SA 15-1 have $^{87}Sr/^{86}Sr$ = 0.707969 and 0.708130,

594   respectively.

6. Discussion

Carbon release to subduction fluids and the mobility of aqueous-carbonic fluids within slabs or along the slab-mantle interface are actively debated topics in considerations of the solid Earth deep C cycle (Ague and Nicolescu, 2014; Berner, 1998; Collins et al., 2015; Cook-Kollars et al., 2014; Dasgupta and Hirschmann, 2010; Epstein et al., 2019; Jaeckel et al., 2018; Kelemen and Manning, 2015; Piccoli et al., 2016; Poli et al., 2009; Poli, 2015; Scambelluri et al., 2016). In this debate, a few studies have considered the geochemical evolution of ophicarbonates by investigating either the C-O isotope compositions of carbonates (Collins et al., 2015; Driesner, 1993; Lafay et al., 2017; Scambelluri et al., 2016; Weissert and Bernoulli, 1984), or the radiogenic isotope and trace element compositions of bulk-rocks and of rock-forming minerals (Miller and Cartwright, 2000; Yamaguchi et al., 2012). Lacking have been studies combining field and petrographic observation, and petrologic work, with trace element concentrations and C, O, and Sr isotope compositions of oceanic and of subduction-zone ophicarbonates aimed at elucidating the geochemical evolution of carbonated serpentinite along the subduction interface. Such studies can build on previous work employing trace elements and Sr isotopes to trace fluid-infiltration in subducting ultramafic rocks (Cannaò et al., 2016, 2015; Harvey et al., 2014). The approach presented in this paper employs such an integration and offers new insight regarding the mechanism of C mobilization in convergent margins.

6.1 Textural and petrologic features

The oceanic ophicarbonates studied here retain serpentine ± magnetite mesh and bastite textures referred to as replacement of former mantle olivine and pyroxenes, respectively (from t_0 to t_2 in **Fig. 9**). During tectonic fragmentation of the serpentinized mantle, carbonation of the bedrock by circulating hydrothermal fluids and accumulation of

621 serpentine clasts in sedimentary-tectonic breccias strongly affected the upper part of the

622 ultramafic sequence (Schwarzenbach et al., 2013; Treves et al., 1995). Calcite formation after

623 the production of the mesh textures (**Fig. 2A**), and along the cleavage of pseudomorph

624 pyroxene, indicates that the mantle protolith was serpentinized prior to carbonation (t3 in **Fig.

625 9**). Calcite formation after serpentinization requires open-system Ca and CO_2 input by the

626 hydrothermal fluids and the release of Si, Mg and water (as hydroxyl molecules – OH^-) into

627 the fluid. Thermodynamic modelling suggests that serpentine replacement by carbonates

628 occurred at 100 °C and 50 MPa at a high activity of CO_2 (Klein and Garrido, 2011). This

629 modelling was confirmed by experimental work showing that formation of calcite or

630 magnesite after serpentinization of peridotite is related to the activity of Mg^{2+} in the fluid and

631 to the presence of relict mantle minerals (Grozeva et al., 2017). Serpentine carbonation can

632 deliver abundant Mg and Si into the hydrothermal system with a consequent increase of the

633 Mg/Ca and Si/Ca of the solutions. In the OCI and OCII ophicarbonates, the absence of Mg-

634 carbonates like dolomite and magnesite, and the only minor $MgCO_3$ component in the calcite,

635 indicates that the hydrothermal fluids reached Mg^{2+} saturation only after full consumption of

636 the aqueous CO_2. In fact, the last carbonation event led to formation of late-stage calcite and

637 talc-bearing veins (**Fig. 2D**). Talc crystallization in such late-stage veins reflects the chemical

638 evolution of hydrothermal fluids through time towards Mg- and Si-rich, and Ca- and CO_2-

639 depleted composition, and marks the end of the oceanic hydrothermal carbonation system (t4

640 in **Fig. 9**). **Figure 10** reports the results of thermodynamic calculations presented as an

641 activity-activity diagram ($\log(a\text{SiO}_2)$ *vs.* $\log(a\text{CO}_2)$) simulating the oceanic carbonation of the

642 pure serpentinite sample MNT 15-1 at low *T* and *P*. The initial carbonation occurs at

643 $\log(a\text{CO}_2)$ values between -11.0 and -7.0 for a $\log(a\text{SiO}_2)$ between -5.0 and -1.8 (red line in

644 **Fig. 10**). In this ranges of $\log(a\text{SiO}_2)$ values, the complete carbonation of relicts of residual

645 mantle minerals (e.g., olivine and pyroxenes) precedes the carbonation of serpentine, the latter

646 occurring at $\log(a\text{CO}_2)$ of -6.0 to -5.0. This process is accompanied by release of H_2O (blue

647 line in **Fig. 10**). At high $\log(a\mathrm{SiO_2})$ values, talc becomes stable (above -1.8, see the green line

648 in **Fig. 10**) over carbonates for a $\log(a\mathrm{CO_2})$ greater than -6.5.

649 The OCI and OCII ophicarbonates showing the highest modal proportions of rocks-

650 forming carbonate also display abundant hematite grains in the carbonated silicate domains

651 and hematite rinds on carbonated clasts (**Fig. 2A, B**; t4 in **Fig. 9**). Overall, these features

652 indicate highly oxidizing condition during carbonation, as also suggested by the formation of

653 hydrous andradite-rich garnet in the bastite textures after former pyroxenes (**Fig. 2C**).

654 The above oceanic transformations created highly oxidized, hydrated, and carbonated

655 serpentinite reservoirs hosting up to 40wt% $\mathrm{CO_2}$ (**Fig. 4**). Subduction of these rocks was

656 accompanied by deformation of the oceanic textures (Stöckhert, 2002) with displacement and

657 recrystallization of coarse oceanic calcite and serpentine along ductile shear zones (**Fig. 3**). At

658 this stage, deformation might have occurred under chemically closed- or open-system

659 conditions. The behaviour of these rocks during subduction can be revealed by textural

660 analysis and study of geochemical markers. With the exception of samples SA 15-1 and SA

661 15-8, the majority of the subducted ophicarbonates for which data are presented here display

662 antigorite + calcite as the main mineral assemblage. Their textures and mineral assemblage

663 could reflect an internal redistribution/recrystallization of minerals and elements inherited

664 from the oceanic stage. However, the pumpellyite- and the blueschist-facies samples are

665 characterized by growth of secondary calcite after the serpentinization of the porphyroclasts

666 displaced along the shear-zone foliation (**Fig. 3B**). The geometry of these clasts suggests syn-

667 tectonic carbonation of serpentine during early subduction stages. Experimental studies

668 showed that the solubility of calcite in $\mathrm{H_2O}$-rich fluid increases with increasing *P-T*

669 conditions of the system (Caciagli and Manning, 2003), suggesting that the carbonation of the

670 serpentinite clasts may have resulted from *in-situ* carbonate dissolution followed by *in-situ*

671 carbonate precipitation. Assuming a closed system condition, the $\mathrm{H_2O}$ required to trigger

672 calcite dissolution may have been derived from the serpentinite clast itself as few wt.% of

673 H2O is released during the serpentine phase transition at increasing *P-T* conditions (Schwartz

674 et al., 2013).

675   Additional textural evidence for C mobility during subduction is provided by the

676 occurrence of carbonate veins crosscutting the eclogite-facies ophicarbonates in the Voltri

677 Massif (LP EOC13-1). Another indication of open system behaviour and infiltration of C-

678 bearing fluids precipitating eclogite-facies magnesite veins is provided by the abundant fluid

679 inclusions hosted by porphyroclastic magnesite of sample SA 15-8. As shown in **Fig. 11D,**

680 and as discussed below, these inclusions shows significant enrichment in FME relative to the

681 concentrations in their magnesite hosts. This might be further evidence for infiltration of C-

682 bearing fluids external to the ophicarbonate host.

683   Taken together, the textures and other observations presented above, for distinct

684 domains in the ophicarbonates we investigated, provide a record of C mobilization over a

685 wide range of *P-T* conditions, beginning on the seafloor and during very early stages of

686 subduction.

687

6.2 Bulk and in-situ trace element features

689   It has been demonstrated that the serpentinization of the oceanic mantle rocks does not

690 strongly modify the REE composition of the peridotite protoliths (Deschamps et al., 2013 and

691 reference therein). The REE composition of the reference serpentinite MNT 15-1 thus

692 reasonably reflects its mantle protolith that is comparable to Internal Liguride (Liguria, Italy)

693 and Monte Maggiore (Corsica, France) peridotites (grey field in **Fig. 5A**; Rampone et al.,

694 2008, 1996). The similarity in the trace element composition of rock-forming serpentine from

695 MNT 15-1 (showing positive B anomaly and depletion in LILE and FME; grey field in **Fig.**

696 **6A**) with other oceanic serpentinites (e.g., Kodolányi et al., 2012) confirms that the alteration

697 process occurred in a marine environment. In contrast, the carbonation of oceanic

698 serpentinites significantly affects REE concentrations (**Fig. 5A**; Allen and Seyfried, 2005).

699 Accordingly, compared to serpentinite MNT 15-1, all of our oceanic ophicarbonates display

700 enrichments in La and variable depletion in Ce (**Fig. 5A**). The oxidation process that occurs

701 during carbonation, revealed by conversion of magnetite to hematite, also affects the

702 behaviour of Ce that, upon oxidized to Ce^{4+}, becomes incompatible in the serpentine and

703 carbonate. Cerium depletion is recorded by the bulk-rock and the mineral *in-situ* analyses of

704 most oceanic ophicarbonates (**Fig. 5A** and **6A**). The enrichment of Ba, B, Cs, U, Pb, As, Sb,

705 Sr, Li in the oceanic ophicarbonates and their rock-forming serpentine and carbonate can be

706 also linked to the carbonation and oxidation of these rocks (Andreani et al., 2014).

707 Enrichment of FME in serpentine may be explained by the alkaline conditions of the

708 hydrothermal environment increasing adsorption of these elements onto the serpentine

709 mineral structure. According to the experimental work by Lafay et al., (2016) the As and Sb

710 enrichments in serpentine (**Fig. 6A**) can be explained when considering that As^{5+} and Sb^{5+} are

711 favourably sequestered by serpentine minerals, compared with As^{3+} and Sb^{3+}, the latter which

712 are mobilized in the fluid phase and/or precipitate as Sb-Ni-accessory phases. For the

713 ophicarbonate calcite, the *in-situ* trace element concentrations are similar to those of

714 serpentine, at least for As that is variably enriched. Uranium is mostly enriched in calcite in

715 the less oxidized sample SG15-4, consistent with its high solubility at elevated oxygen

716 fugacity (e.g., Bailey and Ragnarsdottir, 1994; Keppler and Wyllie, 1991). On the contrary,

717 the Ce concentration in this sample is less depleted, perhaps indicating a key influence of

718 oxygen fugacity in the Ce storage by ophicarbonate minerals.

719 The trace element patterns of the majority of the subducted ophicarbonates, and the

720 minerals therein, do not display significant differences from the patterns in the oceanic

721 samples (**Figs. 5B, D** and **6B, D**). In particular, the coarse and recrystallized calcite in most

722 deformed subduction-related samples do not show significant differences in their trace

723 element budgets (**Fig. 11A, B** and **C**). This evidence suggests that C-mobilization in these

724 samples occurred under closed-system conditions. The main differences in composition of the

725 subduction-related ophicarbonates from the oceanic ones are demonstrated by data for the

726 eclogitic samples SA15-1 and SA 15-8, which show the highest REE concentrations (note the

727 enrichment in LREE relative to MREE and HREE in sample SA15-1, **Fig. 5B**) and higher Pb,

728 As, Sb compared with concentrations in oceanic precursors (**Fig. 5D**). These bulk-rock

729 anomalies are matched by enrichment in Cs, La, Pb, As, Sb of the rock-forming dolomite and

730 calcite (**Figs. 6B** and **D**). Enrichment in these elements in ultramafic rocks have been

731 attributed to exchange with sediment-derived fluids during subduction (Cannaò et al., 2016,

732 2015; Deschamps et al., 2011; Lafay et al., 2013). Therefore, the bulk-rock and *in-situ* trace

733 element data suggest that both closed and open system conditions were experienced by

734 ophicarbonates during the subduction, over their protracted metamorphic histories. In sample

735 SA 15-8, the vein magnesite traps primary and pseudo-secondary inclusions (**Fig. 3G, H**) of

736 the fluid that assisted magnesite growth. As expected, the LA-ICP-MS analyses of inclusion-

737 free and of inclusion-bearing magnesite (**Fig. 11D**) shows that the latter displays much higher

738 Cs, Ba, B, As, Sb, Rb, W, Pb concentrations. This indicates that the fluid carried crustally-

739 derived trace elements, either sourced in subducted sedimentary sequences, or released by

740 dehydration of previously metasomatized altered oceanic crust or associated serpentinites

741 (e.g., Cannaò and Malaspina, 2018 and reference therein).

742

6.3 Tracing C mobility with 3D isotopes

744 The oceanic ophicarbonates studied here, like other oceanic ophicarbonates from the

745 Alps and Pyrenees (e.g., Clerc et al., 2014; Lafay et al., 2017), show wide ranges in O and C

746 isotope compositions (**Fig. 7A**), depending on the *T* of serpentinization and on the amount of

747 reduced C contributing to the $\delta^{13}C$ of the fluids involved (e.g., Alt et al., 2012b; Delacour et

748 al., 2008). In the oceanic ophicarbonates presented here, the O and C isotope compositions of

749 calcite are comparable to published values for the Northern Apennine area (Collins et al.,

750 2015; Galli and Togliatti, 1965; Schwarzenbach et al., 2013). The calcite-seawater isotopic

751 equilibrium indicates that ophicarbonate calcite grew after serpentine over a T range of 130 –

752 110 °C (assuming $\delta^{18}O_{seawater}$ = 0‰, O'Neil et al., 1969) in OCI and OCII. Lower T of about

753 110 – 90 °C were obtained for calcite in veins cross-cutting all oceanic structures in OCI and

754 OCII. These T ranges are comparable to those calculated by Schwarzenbach et al. (2013) for

755 ophicarbonates from the same area (between 150 and 50 °C). All oceanic ophicarbonates

756 presented here preserve a C isotope fingerprint consistent with acquisition of C during

757 interaction with seawater-derived fluids. In OCII rocks, the matrix calcite in less oxidized

758 samples (SG 15-4 and SG 15-2) shows slightly lower $\delta^{13}C$ likely as the result of interaction

759 with serpentinite clasts, showing isotopically negative values (Alt et al., 2012b; Lafay et al.,

760 2017). The high degree of variability in the C-O isotope compositions of the oceanic protolith

761 has to be taken into account when discussing the evolution of ophicarbonates during

762 subduction evolution. The $^{87}Sr/^{86}Sr$ ratios of the oceanic ophicarbonates investigated here and

763 of the pure serpentinite MNT 15-1 range between 0.7060 and 0.7070 (**Fig. 8**): such values

764 approach the value of 0.7070 defined for Jurassic seawater (Jones et al., 1994), consistent

765 with carbonation having involved Jurassic seawater re-equilibrated with a mafic/ultramafic

766 reservoir.

767 Carbonate $\delta^{18}O$ values for the pumpellyite- and of the blueschist-facies ophicarbonates

768 overlap the lower-$\delta^{18}O$ range for OCI and OCII. The T range achieved for calcite

769 crystallization in these rocks, based on $\delta^{18}O$ values, is 130-90 °C (assuming $\delta^{18}O_{seawater}$ = 0‰,

770 O'Neil et al., 1969). Such T are in the range for alteration of the oceanic ophicarbonates,

771 indicating that these ophicarbonates retain the oceanic O isotope imprint of the protolith rocks.

772 Therefore, although subducted ophicarbonates can display either undeformed or deformed

773 textures attributable to dynamic subduction-zone recrystallization, their $\delta^{18}O$ does not require

774 contribution by alteration after seawater-rock interaction. Whereas the O isotope

775 compositions of these rocks are consistent with little or no subduction-related modification of

776 seafloor compositions, the $\delta^{13}C$ values (particularly that of sample CU 13-1) could reflect

777 some modification by high-P metamorphic fluids. The $\delta^{13}C$ values of calcite in the

778 pumpellyite-facies samples and the undeformed blueschist-facies sample CU3 show no

779 significant deviation from the values expected for oceanic ophicarbonates (**Fig. 7B**), despite

780 the sampling of two generations of early (coarse) and later (recrystallized) calcite in these

781 subduction-zone metamorphosed samples (see **Appendix Figure A1**). Coupling this

782 observation with the preservation of the oceanic $\delta^{18}O$, with the $^{87}Sr/^{86}Sr$ signature (**Fig. 8**),

783 and the *in-situ* trace element analyses (**Fig. 11A**) indicates inheritance of the oceanic

784 compositions, at closed-system conditions, during subduction. In contrast, calcite in the

785 deformed sample CU 13-1 has lower negative $\delta^{13}C$ values (from -1 to -2‰, **Fig. 7B**) that can

786 be ascribed to either larger contribution from reduced/organic C during oceanic carbonation

787 or the influence of reduced C during interaction with fluids sourced during subduction from

788 the surrounding metasedimentary rocks (Collins et al., 2015; Cook-Kollars et al., 2014). The

789 more radiogenic Sr isotope composition of CU 13-1 (**Fig. 8**) supports the second scenario (a

790 metasedimentary source), despite the lack of evidence for significant trace element influx

791 from sediments based on the *in-situ* analyses (**Fig. 11B**). Carbon additions from

792 metasedimentary rocks into ultramafic ophicarbonates in the Queyras area has been

793 documented by means of Fe and Zn isotope systematics by Debret et al. (2018), who showed

794 that during subduction, these rocks underwent several stages of carbonate dissolution and

795 precipitation involving sediment-derived fluids.

796   One eclogitic sample from the Voltri Massif (LP13 EOC3) affected by ductile

797 deformation and carbonate recrystallization displays $\delta^{13}C$ and $\delta^{18}O$ overlapping values for the

798 pumpellyite-facies rocks (**Fig. 7B**), suggesting a subduction evolution under closed-system

799 conditions. This interpretation is supported by a lack of enrichment in FME of the

800 recrystallized calcite (**Fig. 11C**) and by low radiogenic Sr, with $^{87}Sr/^{86}Sr$ still compatible with

801 an oceanic fingerprint (**Fig. 8**). In contrast, the other eclogitic samples from Voltri Massif are

802 characterized by the lowest $\delta^{18}O$ (down to +10.5‰, **Fig. 7B**), matching with the compositions

803 of the eclogite-facies ophicarbonates from the Zermatt-Saas Zone (Collins et al., 2015),

804 whereas their $\delta^{13}C$ values are similar to those of the other oceanic and subducted

805 ophicarbonates (**Fig. 7B**). Considering that in these samples, (i) magnesite veins formed

806 during subduction (sample SA 15-8), (ii) dolomite crystallized together with antigorite and

807 diopside under high-*P* conditions (sample SA 15-1), and (iii) calcite veins crosscut the

808 prograde antigorite (sample LP13 EOC1), and assuming that their original $\delta^{18}O$ was the same

809 as that of the oceanic ophicarbonates, the Voltri ophicarbonates are regarded as having re-

810 equilibrated with metamorphic fluids that lowered their seafloor-inherited $\delta^{18}O$ (e.g., Miller

811 and Cartwright, 2000). Decrease in the $\delta^{18}O$ of these samples is coupled with increase in the

812 FME budgets of carbonates (**Fig. 6**) and with the bulk-rock enrichment in radiogenic Sr (**Fig.

813 8**), indicating influx of externally-derived fluids.

814 Carbonic fluids sourced from metasedimentary rocks during prograde subduction

815 should be characterized by high $\delta^{18}O$ and low $\delta^{13}C$, likely with radiogenic $^{87}Sr/^{86}Sr$ reflecting

816 the elevated Rb/Sr of the rocks (Cook-kollars et al., 2014; Yamaguchi et al., 2012). The $\delta^{18}O$

817 values of calcite, dolomite and magnesite in the eclogitic ophicarbonates suggest that the

818 fluids in equilibrium with these minerals should have $\delta^{18}O$ values of +6.7 to +10.5‰ (at peak

819 T of 500 °C), i.e., +3.8 to +2.5‰ lower than the associated minerals (using the $\Delta^{18}O_{carbonate-water}$ of Zheng, 1999). Such isotopic values are compatible with derivation of the fluids from

821 altered oceanic crust and/or serpentinized mantle (Cartwright and Barnicoat, 1999) rather than

822 sedimentary sources (see Jaeckel et al., 2018). However, the Sr isotope ratios of oceanic,

823 mafic crustal reservoirs are generally less radiogenic than values for the ophicarbonates

824 analyzed in this study. The conundrum is possibly solved by associating the isotopic imprints

825 observed in the high-*P* ophicarbonates with interaction with fluids released by devolatilization

826 of hybridized ultramafic rocks bearing some sedimentary signatures. As a related example,

827 Cannaò et al. (2016) demonstrated that interaction of sediment-derived fluids with the Voltri

828 serpentinites caused enrichments in FME and provided radiogenic Sr and Pb. The subduction

829 dehydration of such a hybrid serpentinite could have released hydrous fluids contributing the

830 isotopic signatures to the subduction ophicarbonates analyzed in this study (high $^{87}Sr/^{86}Sr$,

831 low $\delta^{18}O$, FME enrichment). Beginning with serpentinites with + 6 / +8‰ $\delta^{18}O$ (Cannaò et al.,

832 2016; Früh-Green et al., 2001), the fluids released at 400 to 650 °C, corresponding to the

833 temperatures of olivine-in and antigorite-out reactions (Scambelluri et al., 1995), would have

834 $\delta^{18}O$ ranging from +7.2 to +10.8‰. These values are in good agreement with those of the

835 metamorphic fluids in equilibrium with carbonates from the subduction-zone ophicarbonates

836 for which data are presented in this paper. The fluid generated by devolatilization of the

837 serpentinite also would have low C/O ratio (Alt et al., 2012a), enabling retention of the C

838 isotope compositions of the carbonates, even at fairly high fluid-rock ratios, but modifying the

839 $\delta^{18}O$ towards lower values. Alternatively, interaction of fluids derived by de-serpentinization

840 with metasedimentary rocks along their flow paths in the subduction zone, could have led to

841 the hybridized fluid compositions. Other recent studies of extensively veined mafic rocks and

842 Schistes Lustrés adjacent to fault systems though to represent transient subduction interfaces

843 has demonstrated shifts in $\delta^{18}O$ to similar values and invoked infiltration by H_2O-rich fluids

844 generated by dehydration of mafic and/or ultramafic rocks at greater depths (Angiboust et al.,

845 2017; Epstein et al., 2019; Jaeckel et al., 2018).

846

7. Conclusions

848   In this study, we provide petrographic and geochemical constraints regarding fluid-

849 driven C mobility in ophicarbonates representing shallow levels of subduction zones and their

850 equivalents subducted to depths experiencing eclogitic *P-T* conditions. We characterize the

851 sources of these fluids, identifying cases where compositions can be explained by closed-

852 system conditions and others where open-system fluid-rock interaction appears to have been

853 required. We demonstrate that decarbonation and dissolution/precipitation processes

854 operating in ancient subduction zones are best traced using a combination of detailed field and

petrographic observations, FME inventories and C-O and Sr isotope systematics. We suggest that one challenge to our better understanding subduction zone C fluxes is the upscaling of observations from field and geochemical studies of high-*P* metamorphic rocks to consideration of C cycling at Earth's modern consuming margins.

Figure Caption

Figure 1

Simplified geological map of the Western Alps and location of the studied areas (modify after Collins et al., 2015). **(A)** Geological map of Internal Liguride from the Ligurian N. Apennine ophiolite (modified after Treves and Harper, 1994); **(B)** area of study from the Queyras/Ubaye zone (modified after Michard et al., 2004); **(C)** geological map of the Voltri Massif (modified after Cannaò et al., 2016 and reference therein). Locations of the collected samples for all three areas of study together with the respective sample' labels are indicated with the star symbol.

881

Figure 2

Photomicrographs of the tectonic/hydrothermal (OCI) and sedimentary (OCII) ophicarbonates

from the Northern Apennines: **(A)** parallel and **(B)** crossed polarized light microphotographs

of completely carbonated serpentinite clast. Equant calcite grains overgrowing

pseudomorphic serpentine minerals in the cell of mesh texture and a film of hematite grown

along the border, giving them a ghost-like texture (OCI – MNT 13-5). **(C)** Former

porphyroclast of serpentinized pyroxene (i.e., bastite; red dashed line) partially carbonated

coupled with formation of oceanic garnet along the cleavage (OCI – ISC 13-1). **(D)** Talc

aggregates overgrowing coarse grains of calcite in tardive veins. This represents the last

process affecting the oceanic ophicarbonates (OCI – MNT 13-5). **(E)** Boytroidal versus

irregular blocky calcite in vein (OCII – SG15-4). **(F)** Calcite in sedimentary matrix rich in

hematite. Several serpentinite (Serp) clasts with irregular shape are visible (OCII – MNT 15-

2).

Figure 3

Photomicrographs of the subducted ophicarbonates. **(A)** Old elongated and strained calcite

grains, partially recrystallized along grain boundaries. Complete recrystallization of un-

twinned calcites along major shear zone is visible (PL 13-2). **(B)** Re-oriented serpentinite

clast along the shear zone partially carbonated (Carb clast). Relict of twinned calcites are

visible enclosed in recrystallized prograde calcite mylonites (PL 13-2). **(C)** Stretched

serpentinite clast (Serp) with microfractures and pressure shadows filled by syn-tectonic

extensional calcite-fibers (Syn-tect. calcite). Syn-tectonic calcite is probably linked to the

oceanic stage (CU3). **(D)** Dinamic recrystallization of old strained calcite porphyroclasts

producing fine untwinned calcite grains (CU 13-1). **(E)** Green garnet (Andradite) associated

with oxide (Cr-magnetite – Cr-mgt) and calcite along major deformation zone (LP13 EOC1).

907 **(F)** Relict of the high pressure layer with dolomite + diopside + antigorite (SA 15-1). **(G-H)**

908 Primary and pseudo-secondary fluid inclusions (FI) hosted in magnesite (Mgs) from sample

909 SA 15-8.

910

911 **Figure 4**

912 Bulk-rock major element data showing the relationship between CaO, MgO and SiO_2 of

913 ophicarbonate rocks as well as variations in CO_2 and H_2O with respect to MgO and CaO.

914 Oceanic and subducted ophicarbonates fall in between pure serpentinite and limestone end-

915 members.

916

917 **Figure 5**

918 Primitive mantle normalized (McDonough and Sun, 1995) Rare Earth Element (REE) and

919 trace element patterns of ophicarbonates from oceanic **(A, C)** and subduction **(B, D)** stages. In

920 **(A)** the grey field report the range of the peridotites from Internal Liguride (Rampone et al.,

921 1996). In **(B)** and **(D)**, the grey fields represent the REE and trace element pattern of the

922 oceanic ophicarbonate illustrated in **(A)** and **(C)**.

923

924 **Figure 6**

925 Primitive mantle normalized trace elements patterns of serpentine and carbonate from oceanic

926 **(A, C)** and subduction **(B, D)** stages. In **(B)** and **(D)** grey fields represent the trace element

927 variation of the serpentine and calcite from oceanic origin illustrated in **(A)** and **(C)**. Primitive

928 mantle normalization from McDonough and Sun (1995).

929

930 **Figure 7**

931 Oxygen ($\delta^{18}O_{VSMOW}$) and C ($\delta^{13}C_{VPDB}$) isotopic signatures of ophicarbonates from oceanic

932 **(A)** and subduction **(B)** stages. In **(A)** ophicarbonate fields from Bracco, the Pyrenean and

933 Chenaillet (with different grey colours) are shown for comparison (from Collins et al., 2015;

934 Clerc et al., 2014; Lafay et al., 2017). In **(B)** the Queyras and Zermatt-Saas fields are from

935 Collins et al., (2015) whereas Chatillon ophicarbonates field is from Driesner (1993). The

936 complete $\delta^{18}O$ vs. $\delta^{13}C$ dataset is shown in the **Appendix Figure A1** and in the

937 **Supplementary Table S2**.

938

939 **Figure 8**

940 $^{87}Sr/^{86}Sr$ *vs.* $\delta^{18}O_{VSMOW}$ **(A)** and $\delta^{13}C_{VPDB}$ **(B)** of ophicarbonates studied in this work. For

941 comparison the values of the pure oceanic serpentinite and limestone form the Northern

942 Apennines and of the Jurassic seawater are shown (dashed black lines).

943

944 **Figure 9**

945 Cartoon illustrating the sequence of hydration and carbonation/oxidation processes affecting

946 mantle rocks at oceanic conditions. See text for discussion.

947

948 **Figure 10**

949 Activity-activity diagram for Si and CO_2 (log($aSiO_2$) and log(aCO_2), respectively) depicting

950 phase equilibria in the $MgO-CaO-Al_2O_3-SiO_2-H_2O-CO_2$ system at 100 °C and 1500 bar

951 (calculated using the Perple_X software, Connolly (2005) and the internal consistent

952 thermodynamic database of Holland and Powell (1998) and the compensated Redlich-Kwong

953 (CORK) equation of state of Holland and Powell (1991) for H_2O and CO_2 fluids). Key

954 carbonate-in (in red), talc-in (in green) and release H_2O (in blue) boundaries are emphasized.

955 See text for discussion.

956

957 **Figure 11**

Comparison between in situ trace elements data for coarse and recrystallized calcite from pumpelleyite- **(A),** blueschist- **(B)** and eclogite-facies **(C)** samples. Trace element compositions of fluid inclusion – magnesite mixed measurement compared with pure magnesite are reported in **(D)**. Primitive mantle data from McDonough and Sun (1995).

References

Agard, P., Jolivet, L., Goffé, B., 2001. Tectonometamorphic evolution of the Schistes Lustres Complex; implications for the exhumation of HP and UHP rocks in the Western Alps. Bull. la Soc. Geol. Fr. https://doi.org/10.2113/172.5.617

Ague, J.J., Nicolescu, S., 2014. Carbon dioxide released from subduction zones by fluid-mediated reactions. Nat. Geosci. 7, 355–360. https://doi.org/10.1038/ngeo2143

Allen, D.E., Seyfried, W.E., 2005. REE controls in ultramafic hosted MOR hydrothermal systems: an experimental study at elevated temperature and pressure. Geochim. Cosmochim. Acta 69, 675–683.

Alt, J.C., Crispini, L., Gaggero, L., Levine, D., Lavagnino, G., Shanks, P., Gulbransen, C., 2018. Normal faulting and evolution of fluid discharge in a Jurassic seafloor ultramafic-hosted hydrothermal system. Geology 46, 523–526. https://doi.org/10.1130/G40287.1

Alt, J.C., Garrido, C.J., Shanks, W.C.C., Turchyn, A., Padrón-Navarta, J.A., López Sánchez-Vizcaíno, V., Gómez Pugnaire, M.T., Marchesi, C., Sánchez-Vizcaíno, V.L., Pugnaire, M.T.G., 2012a. Recycling of water, carbon, and sulfur during subduction of serpentinites: A stable isotope study of Cerro del Almirez, Spain. Earth Planet. Sci. Lett. 327, 50–60. https://doi.org/10.1016/j.epsl.2012.01.029

Alt, J.C., Schwarzenbach, E.M., Früh-Green, G.L., Shanks, W.C., Bernasconi, S.M., Garrido, C.J., Crispini, L., Gaggero, L., Padrón-Navarta, J.A., Marchesi, C., 2013. The role of serpentinites in cycling of carbon and sulfur: Seafloor serpentinization and subduction metamorphism. Lithos 178, 40–54. https://doi.org/10.1016/j.lithos.2012.12.006

984 Alt, J.C., Shanks, W.C.C., Crispini, L., Gaggero, L., Schwarzenbach, E.M., Früh-Green, G.L.,

985 Bernasconi, S.M., 2012b. Uptake of carbon and sulfur during seafloor serpentinization

986 and the effects of subduction metamorphism in Ligurian peridotites. Chem. Geol. 322–

987 323, 268–277. https://doi.org/10.1016/j.chemgeo.2012.07.009

988 Andreani, M., Escartin, J., Delacour, A., Ildefonse, B., Godard, M., Dyment, J., Fallick, A.E.,

989 Fouquet, Y., 2014. Tectonic structure, lithology, and hydrothermal signature of the

990 rainbow massif (Mid-Atlantic Ridge 36° 14'N). Geochemistry, Geophys. Geosystems.

991 https://doi.org/10.1002/2014GC005269

992 Angiboust, S., Yamato, P., Hertgen, S., Hyppolito, T., Bebout, G.E., Morales, L., 2017. Fluid

993 pathways and high-P metasomatism in a subducted continental slice (Mt. Emilius klippe,

994 W. Alps). J. Metamorph. Geol. 35, 471–492. https://doi.org/10.1111/jmg.12241

995 Bailey, E.H., Ragnarsdottir, K. V, 1994. Uranium and Thorium Solubilities in Subduction

996 Zone (Vol 124, Pg 119, 1994). Earth Planet. Sci. Lett. 128, 705–706.

997 Barbieri, M., Masi, U., Tolomeo, L., 1979. Stable isotope evidence for a marine origin of

998 ophicalcites from the north-central Apennines (Italy). Mar. Geol. 30, 193–204.

999 https://doi.org/10.1016/0025-3227(79)90015-X

1000 Berner, R.A., 1998. The carbon cycle and CO2 over Phanerozoic time: The role of land plants.

1001 Philos. Trans. R. Soc. B Biol. Sci. 353, 75–82. https://doi.org/10.1098/rstb.1998.0192

1002 Bonatti, E., 1976. Serpentinite protrusions in the oceanic crust. Earth Planet. Sci. Lett. 32,

1003 107–113.

1004 Caciagli, N.C., Manning, C.E., 2003. The solubility of calcite in water at 6-16 kbar and 500-

1005 800 °C. Contrib. to Mineral. Petrol. 146, 275–285. https://doi.org/10.1007/s00410-003-

1006 0501-y

1007 Cannaò, E., Agostini, S., Scambelluri, M., Tonarini, S., Godard, M., 2015. B, Sr and Pb

1008 isotope geochemistry of high-pressure Alpine metaperidotites monitors fluid-mediated

1009 element recycling during serpentinite dehydration in subduction mélange (Cima di

Gagnone, Swiss Central Alps). Geochim. Cosmochim. Acta 163, 80–100.

https://doi.org/10.1016/j.gca.2015.04.024

Cannaò, E., Malaspina, N., 2018. From oceanic to continental subduction : Implications for

the geochemical and redox evolution of the supra-subduction mantle 14.

https://doi.org/10.1130/GES01597.1/4457636/ges01597.pdf

Cannaò, E., Scambelluri, M., Agostini, S., Tonarini, S., Godard, M., 2016. Linking

serpentinite geochemistry with tectonic evolution at the subduction plate-interface: The

Voltri Massif case study (Ligurian Western Alps, Italy). Geochim. Cosmochim. Acta

190, 115–133. https://doi.org/10.1016/j.gca.2016.06.034

Carpena, J., Caby, R., 1984. Fission-track evidence for Late Triassic oceanic crust in the

French Occidental Alps. Geology. https://doi.org/10.1130/0091-

7613(1984)12<108:FEFLTO>2.0.CO;2

Cartwright, I., Barnicoat, A.C., 1999. Stable isotope geochemistry of Alpine ophiolites: A

window to ocean-floor hydrothermal alteration and constraints on fluid-rock interaction

during high-pressure metamorphism. Int. J. Earth Sci. 88, 219–235.

https://doi.org/10.1007/s005310050261

Chiesa, S., Cortesogno, L., Forcella, F., Galli, M., Messiga, B., Pasquaré, G., Pedemonte,

G.M., Piccardo, G.B., Rossi, P.M., 1975. Assetto strutturale ed interpretazione

geodinamica del Gruppo di Voltri. Boll. Soc. Geol. Ital. 94, 555–581.

Cimmino, F., Messiga, B., Piccardo, G.B., Zeda, O., 1979. Titanian clinohumite-bearing

assemblages within antigoritic serpentinitesof the Voltri Massif (Western Liguria):

interferences on the geodynaminc evolution of piemontese ultramafic sections. Ofioliti 4,

97–120.

Clerc, C., Boulvais, P., Lagabrielle, Y., Blanquat, M.D. Saint, 2014. Ophicalcites from the

northern Pyrenean belt : a field , petrographic and stable isotope study 141–163.

https://doi.org/10.1007/s00531-013-0927-z

Collins, N.C., Bebout, G.E., Angiboust, S., Agard, P., Scambelluri, M., Crispini, L., John, T., 2015. Subduction zone metamorphic pathway for deep carbon cycling : II . Evidence from HP / UHP metabasaltic rocks and ophicarbonates. Chem. Geol. 412, 132–150. https://doi.org/10.1016/j.chemgeo.2015.06.012

Connolly, J.A.D., 2005. Computation of phase equilibria by linear programming : A tool for geodynamic modeling and its application to subduction zone decarbonation 236, 524–541. https://doi.org/10.1016/j.epsl.2005.04.033

Cook-Kollars, J., Bebout, G.E., Collins, N.C., Angiboust, S., Agard, P., 2014. Subduction zone metamorphic pathway for deep carbon cycling: I. Evidence from HP/UHP metasedimentary rocks, Italian Alps. Chem. Geol. 386, 31–48. https://doi.org/10.1016/j.chemgeo.2014.07.013

Cortesogno, L., Galbiati, B., Principi, G., 1980. Le brecce serpentinitiche giurassiche della Liguria orientale. Arch. Sci. Genève 33, 185–200.

Cortesogno, L., Lucchetti, G., Massa, B., 1981. Rocce oficarbonate e marmi a silicati nel Massiccio di Voltri: origine e significato, chimismo dei minerali ed equilibri paragenetici. Rend. Soc. Ital. di Mineral. e Petrol. 37, 481–507.

Crispini, L., Capponi, G., 2001. Tectonic evolution of the Voltri Group and Sestri Voltaggio Zone (southern limit of the NW Alps): a review. Ofioliti 26, 161–164.

Dasgupta, R., Hirschmann, M.M., 2010. The deep carbon cycle and melting in Earth ' s interior. Earth Planet. Sci. Lett. 298, 1–13. https://doi.org/10.1016/j.epsl.2010.06.039

Debret, B., Bouilhol, P., Pons, M.L., Williams, H., 2018. Carbonate transfer during the onset of slab devolatilization: New insights from fe and Zn stable isotopes. J. Petrol. 59, 1145–1166. https://doi.org/10.1093/petrology/egy057

Decandia, F.A., Lazzarotto, A., Liotta, D., Cernobori, L., Nicolich, R., 1998. The CROP3 traverse: insights on post-collisional evolution of Northern Apennines.

Delacour, A., Früh-Green, G.L., Frank, M., Gutjahr, M., Kelley, D.S., 2008. Sr-and Nd-

isotope geochemistry of the Atlantis Massif (30 N, MAR): implications for fluid fluxes and lithospheric heterogeneity. Chem. Geol. 254, 19–35.

Deschamps, F., Godard, M., Guillot, S., Hattori, K., 2013. Geochemistry of subduction zone serpentinites: A review. Lithos 178, 96–127. https://doi.org/10.1016/j.lithos.2013.05.019

Deschamps, F., Guillot, S., Godard, M., Andreani, M., Hattori, K., 2011. Serpentinites act as sponges for fluid-mobile elements in abyssal and subduction zone environments. Terra Nov. 23, 171–178.

Driesner, T., 1993. Aspects of Petrographic, Structural and Stable Isotope Geochemical Evolution of Ophicarbonate Breccias from Ocean-Floor to Subduction and Uplift - an Example from Chatillon, Middle Aosta Valley, Italian Alps. Schweizerische Mineral. Und Petrogr. Mitteilungen 73, 69–84.

Epstein, G., Angiboust, S., Bebout, G., 2019. Scales of Fluid-Rock Interaction and Carbon Mobility in the Deeply Underplated and HP -Metamorphosed Schistes Lustrés , Western Alps. LITHOS 105229. https://doi.org/10.1016/j.lithos.2019.105229

Federico, L., Capponi, G., Crispini, L., Scambelluri, M., 2004. Exhumation of alpine high-pressure rocks: Insights from petrology of eclogite clasts in the Tertiary Piedmontese basin (Ligurian Alps, Italy). Lithos 74, 21–40. https://doi.org/10.1016/j.lithos.2003.12.001

Federico, L., Crispini, L., Scambelluri, M., Capponi, G., 2007. Ophiolite melange zone records exhumation in a fossil subduction channel. Geology 35, 499–502. https://doi.org/10.1130/G23190A.1

Frezzotti, M.L., Selverstone, J., Sharp, Z.D., Compagnoni, R., 2011. Carbonate dissolution during subduction revealed by diamond-bearing rocks from the Alps. Nat. Geosci. 4, 703–706. https://doi.org/10.1038/ngeo1246

Früh-Green, G.L., Connolly, J.A.D., Plas, A., Kelley, D.S., Grobety, B., 2004. Serpentinization of Oceanic Peridotites : Implications for Geochemical Cycles and

1088   Biological Activity The Subseafloor Biosphere at Mid-Ocean Ridges. Geophys. Monogr.

1089   Ser. 144, 119–136.

1090   Früh-Green, G.L., Scambelluri, M., Vallis, F., 2001. O-H isotope ratios of high pressure

1091   ultramafic rocks: Implications for fluid sources and mobility in the subducted hydrous

1092   mantle. Contrib. to Mineral. Petrol. 141, 145–159.

1093   https://doi.org/10.1007/s004100000228

1094   Früh-Green, G.L., Weissert, H., Bernoulli, D., 1990. A multiple fluid history recorded in

1095   Alpine ophiolites. J. Geol. Soc. London. 147, 959–970.

1096   https://doi.org/10.1144/gsjgs.147.6.0959

1097   Galli, M., 1957. Il Rosso di Levanto. Rend. Soc. Miner. Ital 13, 265–267.

1098   Galli, M., Togliatti, V., 1965. Ricerche petrografiche sulla formazione ofiolitica

1099   dell'Appennino Ligure. Il Rosso di Levanto—nuovo contributo. Ann. Mus. Civ. St. Nat.

1100   Genova 75, 359–381.

1101   Godard, M., Jousselin, D., Bodinier, J.-L., 2000. Relationships between geochemistry and

1102   structure beneath a palaeo-spreading centre: a study of the mantle section in the Oman

1103   ophiolite. Earth Planet. Sci. Lett. 180, 133–148.

1104   Grozeva, N.G., Klein, F., Seewald, J.S., Sylva, S.P., 2017. Experimental study of carbonate

1105   formation in oceanic peridotite. Geochim. Cosmochim. Acta 199, 264–286.

1106   https://doi.org/10.1016/j.gca.2016.10.052

1107   Guillong, M., Meier, D.L., Allan, M.M., Heinrich, C.A., Yardley, B.W.D., 2008. Appendix

1108   A6: SILLS: a MATLAB-based program for the reduction of laser ablation ICP-MS data

1109   of homogeneous materials and inlusions 328–333.

1110   Halter, W.E., Pettke, T., Heinrich, C.A., Rothen-Rutishauser, B., 2002. Major to trace element

1111   analysis of melt inclusions by laser-ablation ICP-MS: Methods of quantification. Chem.

1112   Geol. 183, 63–86. https://doi.org/10.1016/S0009-2541(01)00372-2

1113   Harvey, J., Garrido, C.J., Savov, I.P., Agostini, S., Padrón-Navarta, J.A., Marchesi, C.,

1114   Sánchez-Vizcaíno, V.L., Gómez-Pugnaire, M.T., 2014. 11 B-rich fluids in subduction

1115   zones: The role of antigorite dehydration in subducting slabs and boron isotope

1116   heterogeneity in the mantle. Chem. Geol. 376, 20–30.

1117 Hermann, J., Müntener, O., Scambelluri, M., Mu, O., 2000. The importance of serpentinite

1118   mylonites for subduction and exhumation of oceanic crust. Tectonophysics 327, 225–

1119   238. https://doi.org/10.1016/S0040-1951(00)00171-2

1120 Holland, T., Powell, R., 1991. A Compensated-Redlich-Kwong (CORK) equation for

1121   volumes and fugacities of CO2 and H2O in the range 1 bar to 50 kbar and 100-1600°C.

1122   Contrib. to Mineral. Petrol. https://doi.org/10.1007/BF00306484

1123 Holland, T.J.B., Powell, R., 1998. An internally consistent thermodynamic data set for phases

1124   of petrological interest. J. Metamorph. Geol. 16, 309–343.

1125   https://doi.org/10.1111/j.1525-1314.1998.00140.x

1126 Hoogerduijn Strating, E.H., Rampone, E., Piccardo, G.B., Drury, M.R., Vissers, R.L.M., 1993.

1127   Subsolidus emplacement of mantle peridotites during incipient oceanic rifting and

1128   opening of the Mesozoic Tethys (Voltri Massif, NW Italy). J. Petrol. 34, 901–927.

1129 Ionov, D.A., Savoyant, L., Dupuy, C., 1992. Application of the ICP-MS techmique to trace

1130   element analysis of peridotite and their minerals. Geostand. Newsl. 16, 311–315.

1131 Jaeckel, K., Bebout, G.E., Angiboust, S., 2018. Deformation-enhanced fluid and mass transfer

1132   along Western and Central Alps paleo-subduction interfaces: Significance for carbon

1133   cycling models. Geosphere 14, 2355–2375. https://doi.org/10.1130/GES01587.1

1134 Jochum, K.P., Nohl, U., Herwig, K., Lammel, E., Stoll, B., Hofmann, A.W., 2005. GeoReM:

1135   A New Geochemical Database for Reference Materials and Isotopic Standards. Geostand.

1136   Geoanalytical Res. 29, 333–338. https://doi.org/10.1111/j.1751-908x.2005.tb00904.x

1137 Jones, C.E., Jenkyns, H.C., Coe, A.L., Stephen, H.P., 1994. Strontium isotopic variations in

1138   Jurassic and Cretaceous seawater. Geochim. Cosmochim. Acta 58, 3061–3074.

1139 Kelemen, P.B., Manning, C.E., 2015. Reevaluating carbon fluxes in subduction zones, what

1140   goes down, mostly comes up. Proc. Natl. Acad. Sci. 112, E3997–E4006.

1141   https://doi.org/10.1073/pnas.1507889112

1142   Kelley, D.S., Karson, J.A., Fru, G.L., Yoerger, D.R., Shank, T.M., Butterfield, D.A., Hayes,

1143   J.M., Schrenk, M.O., Olson, E.J., Proskurowski, G., Jakuba, M., Bradley, A., Larson, B.,

1144   Ludwig, K., Glickson, D., Buckman, K., Bradley, A.S., Brazelton, W.J., Roe, K.,

1145   Bernasconi, S.M., Elend, M.J., Lilley, M.D., Baross, J.A., Summons, R.E., Sylva, S.P.,

1146   2005. Kelley_05 307, 1–7.

1147   Keppler, H., Wyllie, P.J., 1991. Partitioning of Cu, Sn, Mo, W, U, and Th between melt and

1148   aqueous fluid in the systems haplogranite-H2O-HCl and haplogranite-H2O-HF. Contrib.

1149   to Mineral. Petrol. https://doi.org/10.1007/BF00306474

1150   Kerrick, D.M., Connolly, J.A.D., 2001. Metamorphic devolatilization of subducted marine

1151   sediments and the transport of volatiles into the Earth ' s mantle 36, 293–296.

1152   Kerrick, D.M., Connolly, J.A.D., 1998. Subduction of ophicarbonates and recycling of CO2

1153   and H2O. Geology 26, 375–378.

1154   Klein, F., Garrido, C.J., 2011. Thermodynamic constraints on mineral carbonation of

1155   serpentinized peridotite. Lithos 126, 147–160.

1156   https://doi.org/10.1016/j.lithos.2011.07.020

1157   Kodolányi, J., Pettke, T., Spandler, C., Kamber, B.S., Ling, K.G., Gme, K., 2012.

1158   Geochemistry of ocean floor and fore-arc serpentinites: Constraints on the ultramafic

1159   input to subduction zones. J. Petrol. 53, 235–270.

1160   https://doi.org/10.1093/petrology/egr058

1161   Lafay, R., Baumgartner, L.P., Stephane, S., Suzanne, P., German, M.H., Torsten, V., 2017.

1162   Petrologic and stable isotopic studies of a fossil hydrothermal system in ultramafic

1163   environment (Chenaillet ophicalcites, Western Alps, France): Processes of carbonate

1164   cementation. Lithos 294–295, 319–338. https://doi.org/10.1016/j.lithos.2017.10.006

1165   Lafay, R., Deschamps, F., Schwartz, S., Guillot, S., Godard, M., Debret, B., Nicollet, C., 2013.

High-pressure serpentinites, a trap-and-release system controlled by metamorphic

conditions: Example from the Piedmont zone of the western Alps. Chem. Geol. 343, 38–

54.

Lafay, R., Montes-Hernandez, G., Janots, E., Munoz, M., Auzende, A.L., Gehin, A., Chiriac,

R., Proux, O., 2016. Experimental investigation of As, Sb and Cs behavior during olivine

serpentinization in hydrothermal alkaline systems. Geochim. Cosmochim. Acta 179,

177–202. https://doi.org/10.1016/j.gca.2016.02.014

Lagabrielle, Y., 1987. Les ophiolites: marqueurs de l'histoire tectonique des domaines

océaniques: le cas des Alpes franco-italiennes (Queyras, Piémont). Brest.

Lagabrielle, Y., Lemoine, M., Tricart, P., 1985. Paléotectonique océanique et déformations

alpines dans le massif ophiolitique du Pelvas d'Abriès (Alpes Occidentales-Queyras-

France). Bull. la Société Géologique Fr. 1, 473–480.

Lemoine, M., Tricart, P., Boillot, G., 1987. Ultramafic and gabbroic ocean floor of the

Ligurian Tethys (Alps, Corsica, Apennines): in search of a genetic model. Geology 15,

622–625. https://doi.org/10.1130/0091-7613(1987)15<622:UAGOFO>2.0.CO;2

Leoni, L., Marroni, M., Sartori, F., Tamponi, M., 1996. Metamorphic grade in metapelites of

the Internal Liguride Units (Northern Apennines, Italy). Eur. J. Mineral. 8, 70176.

https://doi.org/10.1127/ejm/8/1/0035

Ludwig, K.A., Kelley, D.S., Butterfield, D.A., Nelson, B.K., Früh-Green, G.L., 2006.

Formation and evolution of carbonate chimneys at the Lost City Hydrothermal Field.

Geochim. Cosmochim. Acta 70, 3625–3645. https://doi.org/10.1016/j.gca.2006.04.016

Malaspina, N., Poli, S., Fumagalli, P., 2009. The oxidation state of metasomatized mantle

wedge: Insights from C-O-H-bearing garnet peridotite. J. Petrol. 50, 1533–1552.

https://doi.org/10.1093/petrology/egp040

Malatesta, C., Crispini, L., Federico, L., Capponi, G., Scambelluri, M., 2012. The exhumation

of high pressure ophiolites (Voltri Massif, Western Alps): Insights from structural and

1192   petrologic data on metagabbro bodies. Tectonophysics 568–569, 102–123.

1193   https://doi.org/10.1016/j.tecto.2011.08.024

1194   McCrea, J.M., 1950. On the isotopic chemistry of carbonates and a paleotemperature scale. J.

1195   Chem. Phys. https://doi.org/10.1063/1.1747785

1196   McDonough, W.F., Sun, S.-S., 1995. The composition of the Earth. Chem. Geol. 120, 223–

1197   253.

1198   Messiga, B., Scambelluri, M., 1991. Retrograde P-T-T path for the Voltri-Massif eclogites

1199   (Ligurian Alps, Italy) - some tectonic implications. J. Metamorph. Geol. 9, 93–109.

1200   Mével, C., 2003. Serpentinization of abyssal peridotites at mid-ocean ridges. Comptes Rendus

1201   Geosci. 335, 825–852.

1202   Michard, A., Goffé, B., Avigad, D., 2004. The high-pressure metamorphic front of the south

1203   Western Alps (Ubaye-Maira transect, France, Italy). Schweizerische Mineral. und

1204   Petrogr. Mitteilungen 84, 215–235.

1205   Miller, J.A., Cartwright, I., 2000. Distinguishing between seafloor alteration and fluid flow

1206   during subduction using stable isotope geochemistry: Examples from Tethyan ophiolites

1207   in the Western Alps. J. Metamorph. Geol. 18, 467–482. https://doi.org/10.1046/j.1525-

1208   1314.2000.00274.x

1209   Molina, J.F., Poli, S., 2000. Carbonate stability and fluid composition in subducted oceanic

1210   crust: An experimental study on H_2O-CO_2-bearing basalts. Earth Planet. Sci. Lett. 176,

1211   295–310. https://doi.org/10.1016/S0012-821X(00)00021-2

1212   O'Hanley, D.S., 1996. Serpentinites. Oxford University Press on Demand.

1213   O'Neil, J.R., Clayton, R.N., Mayeda, T.K., 1969. Oxygen isotope fractionation in divalent

1214   metal carbonates. J. Chem. Phys. 51, 5547–5558. https://doi.org/10.1063/1.1671982

1215   Paul, D., Skrzypek, G., 2007. Assessment of carbonate-phosphoric acid analytical technique

1216   performed using GasBench II in continuous flow isotope ratio mass spectrometry. Int. J.

1217   Mass Spectrom. https://doi.org/10.1016/j.ijms.2006.11.006

Peters, D., Pettke, T., 2017. Evaluation of Major to Ultra Trace Element Bulk Rock Chemical

    Analysis of Nanoparticulate Pressed Powder Pellets by LA-ICP-MS. Geostand.

    Geoanalytical Res. 41, 5–28. https://doi.org/10.1111/ggr.12125

Pettke, T., Oberli, F., Audétat, A., Guillong, M., Simon, A.C., Hanley, J.J., Klemm, L.M.,

    2012. Recent developments in element concentration and isotope ratio analysis of

    individual fluid inclusions by laser ablation single and multiple collector ICP-MS. Ore

    Geol. Rev. https://doi.org/10.1016/j.oregeorev.2011.11.001

Piccoli, F., Vitale, A., Beyssac, O., Martinez, I., Ague, J.J., Chaduteau, C., 2016. Carbonation

    by fluid – rock interactions at high-pressure conditions : Implications for carbon cycling

    in subduction zones. Earth Planet. Sci. Lett. 1, 1–14.

    https://doi.org/10.1016/j.epsl.2016.03.045

Poli, S., 2015. Carbon mobilized at shallow depths in subduction zones by carbonatitic liquids.

    Nat. Geosci. 8, 633–636. https://doi.org/10.1038/ngeo2464

Poli, S., Franzolin, E., Fumagalli, P., Crottini, A., 2009. The transport of carbon and hydrogen

    in subducted oceanic crust: An experimental study to 5 GPa. Earth Planet. Sci. Lett. 278,

    350–360. https://doi.org/10.1016/j.epsl.2008.12.022

Rampone, E., Hofmann, A.W., Piccardo, G.B., Vannucci, R., Bottazzi, P., Ottolini, L.,

    Hofmann, W., Piccardo, B., Vannucci, R., Bottazzi, P., Ottolini, L., 1996. Trace element

    and isotope geochemistry of depleted peridotites from an N-MORB type ophiolite

    (Internal Liguride, N. Italy). Contrib. to Mineral. Petrol. 123, 61–76.

    https://doi.org/10.1007/s004100050143

Rampone, E., Piccardo, G.B., Hofmann, A.W., 2008. Multi-stage melt-rock interaction in the

    Mt. Maggiore (Corsica, France) ophiolitic peridotites: Microstructural and geochemical

    evidence. Contrib. to Mineral. Petrol. 156, 453–475. https://doi.org/10.1007/s00410-008-

    0296-y

Sapienza, G.T., Scambelluri, M., Braga, R., 2009. Dolomite-bearing orogenic garnet

1244   peridotites witness fluid-mediated carbon recycling in a mantle wedge (Ulten Zone,

1245   Eastern Alps, Italy). Contrib. to Mineral. Petrol. 158, 401–420.

1246   https://doi.org/10.1007/s00410-009-0389-2

1247 Scambelluri, M., Bebout, G.E., Belmonte, D., Gilio, M., Campomenosi, N., Collins, N.,

1248   Crispini, L., 2016. Carbonation of subduction-zone serpentinite (high-pressure

1249   ophicarbonate ; Ligurian Western Alps) and implications for the deep carbon cycling.

1250   Earth Planet. Sci. Lett. 441, 155–166. https://doi.org/10.1016/j.epsl.2016.02.034

1251 Scambelluri, M., Hoogerduijn Strating, E.H., Piccardo, G.B., Vissers, R.L.M., Rampone, E.,

1252   1991. Alpine olivine- and titanian clinohumite-bearing assemblages in the Erro-Tobbio

1253   peridotite (Voltri Massif, NW Italy). J. Metamorph. Geol. 9, 79–91.

1254 Scambelluri, M., Muntener, O., Hermann, J., Piccardo, G.B., Trommsdorff, V., 1995.

1255   Subduction of water into the mantle: history of an Alpine peridotite. Geology.

1256   https://doi.org/10.1130/0091-7613(1995)023<0459:SOWITM>2.3.CO;2

1257 Scambelluri, M., Tonarini, S., 2012. Boron isotope evidence for shallow fluid transfer across

1258   subduction zones by serpentinized mantle. Geology 40, 907–910.

1259 Schwartz, S., Guillot, S., Reynard, B., Lafay, R., Debret, B., Nicollet, C., Lanari, P., Auzende,

1260   A.L., 2013. Pressure temperature estimates of the lizardite/antigorite transition in high

1261   pressure serpentinites. Lithos 178, 197–210.

1262 Schwarzenbach, E.M., Früh-Green, G.L., Bernasconi, S.M., Alt, J.C., Plas, A., 2013.

1263   Serpentinization and carbon sequestration: A study of two ancient peridotite-hosted

1264   hydrothermal systems. Chem. Geol. 351, 115–133.

1265   https://doi.org/10.1016/j.chemgeo.2013.05.016

1266 Sharma, S. Das, Patil, D.J., Gopalan, K., 2002. Temperature dependence of oxygen isotope

1267   fractionation of CO_2 from magnesite-phosphoric acid reaction. Geochim. Cosmochim.

1268   Acta. https://doi.org/10.1016/S0016-7037(01)00833-X

1269 Spandler, C., Pettke, T., Rubatto, D., 2011. Internal and External Fluid Sources for Eclogite-

facies Veins in the Monviso Meta-ophiolite, Western Alps: Implications for Fluid Flow

in Subduction Zones. J. Petrol. 52, 1207–1236. https://doi.org/10.1093/petrology/egr025

Stöckhert, B., 2002. Stress and deformation in subduction zones: insight from the record of

exhumed metamorphic rocks. Geol. Soc. London, Spec. Publ.

https://doi.org/10.1144/gsl.sp.2001.200.01.15

Tartarotti, P., Guerini, S., Rotondo, F., Festa, A., Balestro, G., Bebout, G.E., Cannaò, E.,

Epstein, G.S., Scambelluri, M., 2019. Superposed Sedimentary and Tectonic Block-In-

Matrix Fabrics in a Subducted Serpentinite Mélange (High-Pressure Zermatt Saas

Ophiolite , Western Alps). Geosciences 9, 1–29.

https://doi.org/10.3390/geosciences9080358

Treves, B., Hickmott, D., Vaggelli, G., 1995. Texture and microchemical data of oceanic

hydrothermal calcite veins, northern Apennine ophicalcites. Ofioliti 20, 111–122.

Treves, B.E., Harper, G.D., 1994. Exposure of serpentinites on the ocean floor: sequence of

faulting and hydrofracturing in the northern Apennine ophicalcites. Ofioliti.

Tricart, P., Lemoine, M., 1991. The Queyras ophiolite West of Monte Viso (Western Alps):

Indicator of a pecular ocean floor in the mesozoic tethys. J. Geodyn.

https://doi.org/10.1016/0264-3707(91)90037-F

Vissers, R.L.M., Drury, M.R., Hoogerduijn^Strating, E.H., Spiers, C.J., van der Wal, D., 1995.

Mantle shear zones and their effect on lithosphere strength during continental breakup.

Tectonophysics. https://doi.org/10.1016/0040-1951(95)00033-J

Vissers, R.L.M., Drury, M.R., Strating, E.H.H., der Wal, D., 1991. Shear zones in the upper

mantle: A case study in an Alpine Iherzolite massif. Geology 19, 990–993.

Weissert, H., Bernoulli, D., 1984. Oxygen isotope composition of calcite in Alpine

ophicarbonates: a hydrothermal or Alpine metamorphic signal? Eclogae Geol. Helv. 77/1,

29–43.

Yamaguchi, A., Ujiie, K., Nakai, S., Kimura, G., 2012. Sources and physicochemical

characteristics of fluids along a subduction-zone megathrust: A geochemical approach using syn-tectonic mineral veins in the Mugi mélange, Shimanto accretionary complex. Geochemistry, Geophys. Geosystems 13. https://doi.org/10.1029/2012GC004137

1
2
3
4
5
6
7
8
9
10
11
12
13
14
15
16
17
18
19
20
21
22
23
24
25
26
27
28
29
30
31
32
33
34
35
36
37
38
39
40
41
42
43
44
45
46
47
48
49
50
51
52
53
54
55
56
57
58
59
60
61
62
63
64
65

Figure 1
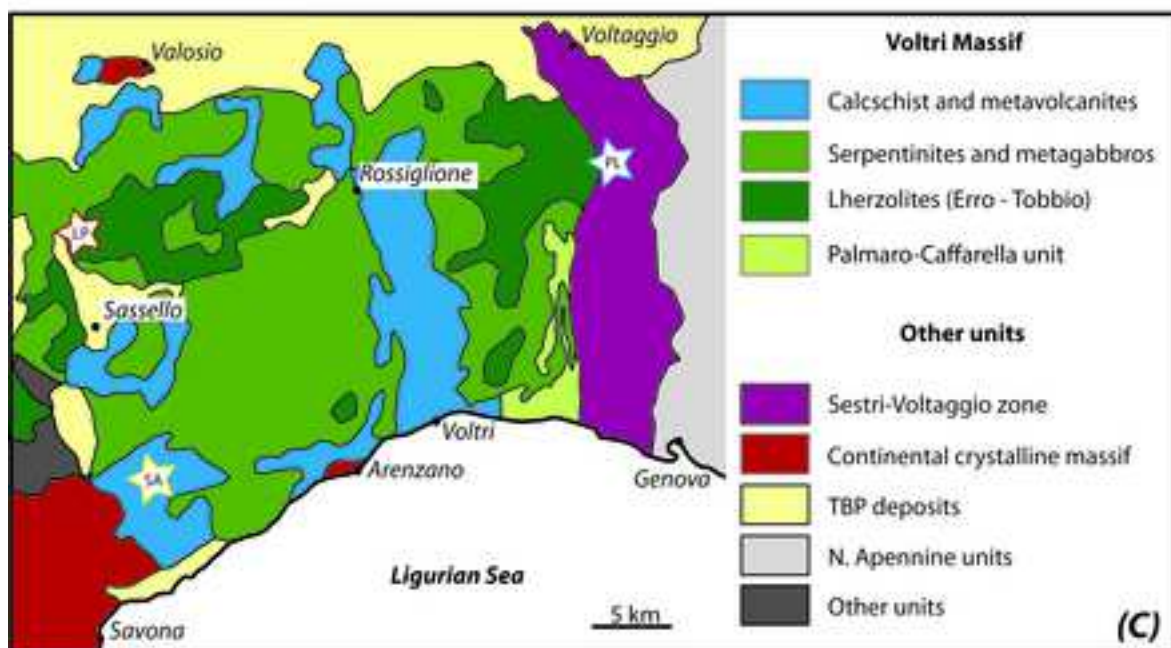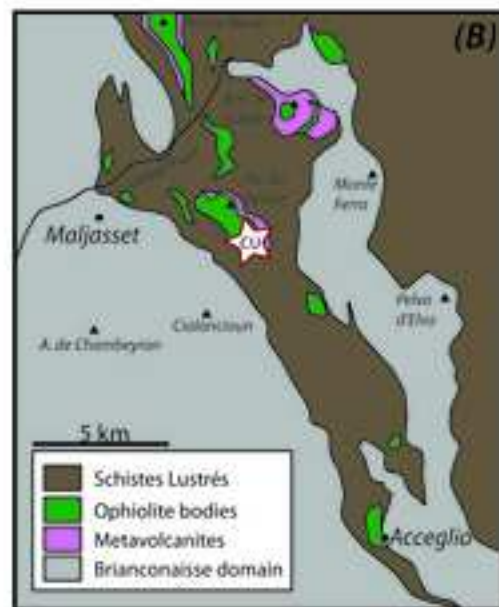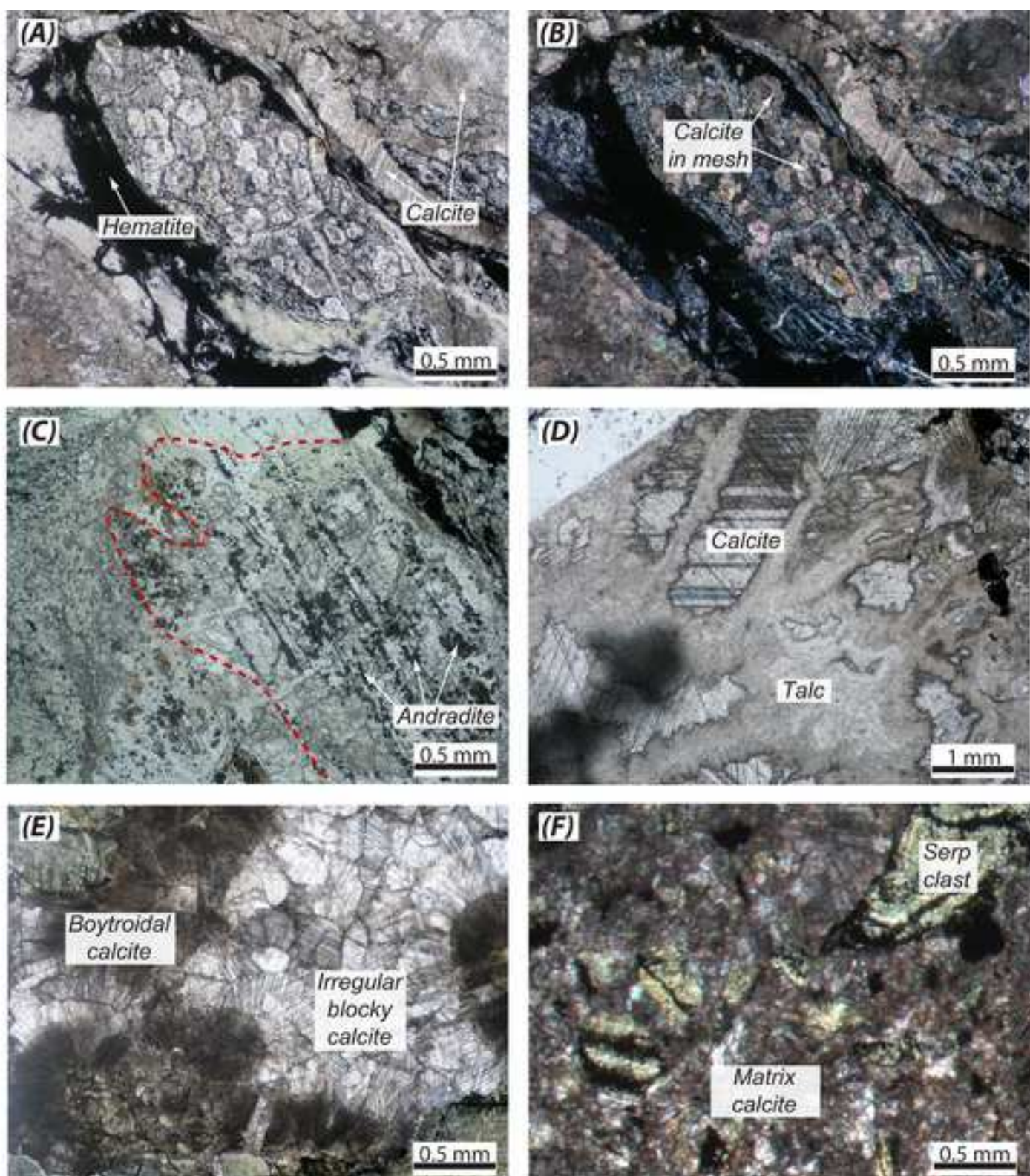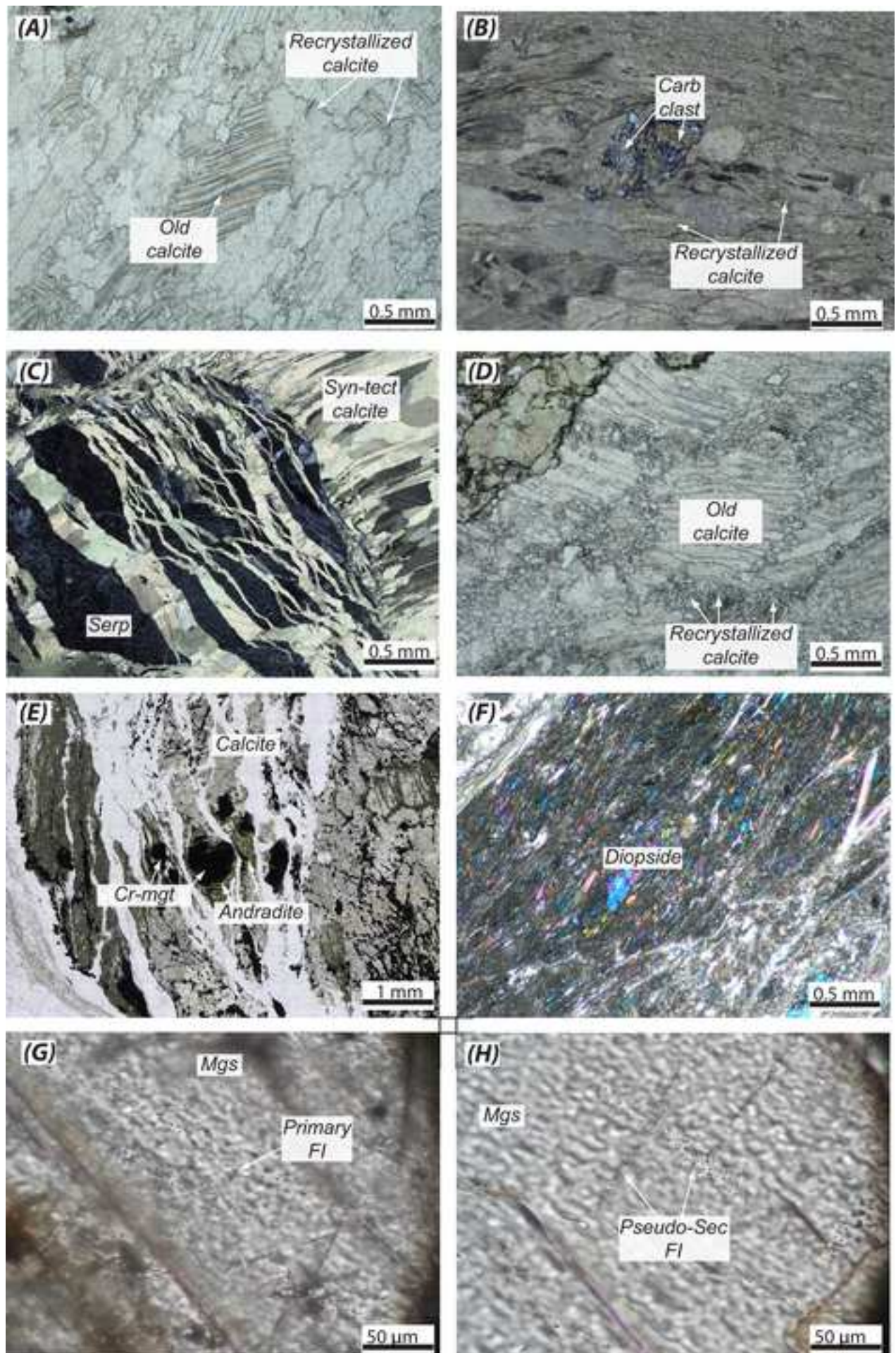**Click here to download high resolution image**

Figure 3
[Click here to download high resolution image](#)

Figure 4
[Click here to download high resolution image](#)
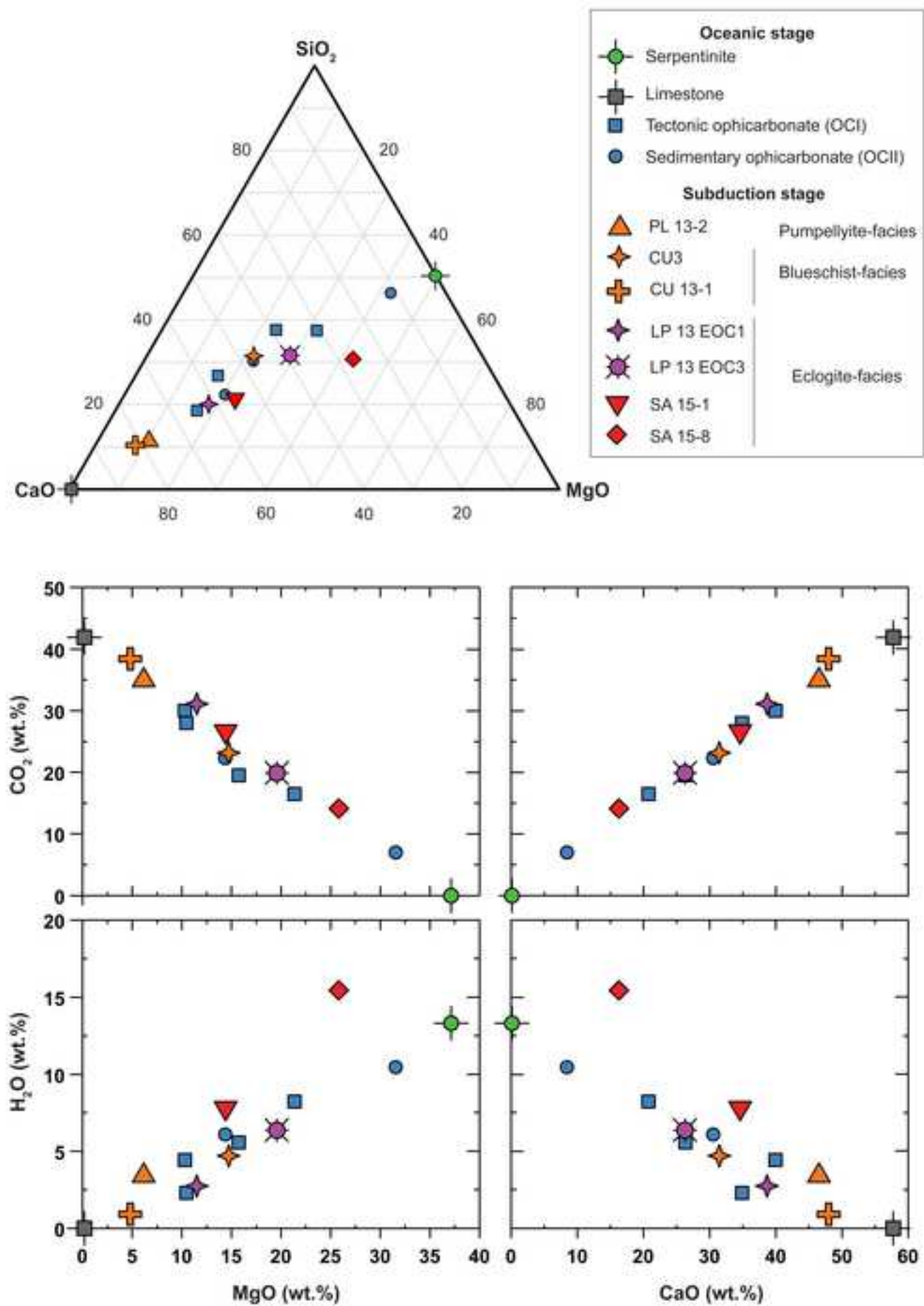
Figure 5

Figure 6
Click here to download high resolution image

Figure 7

Figure 10
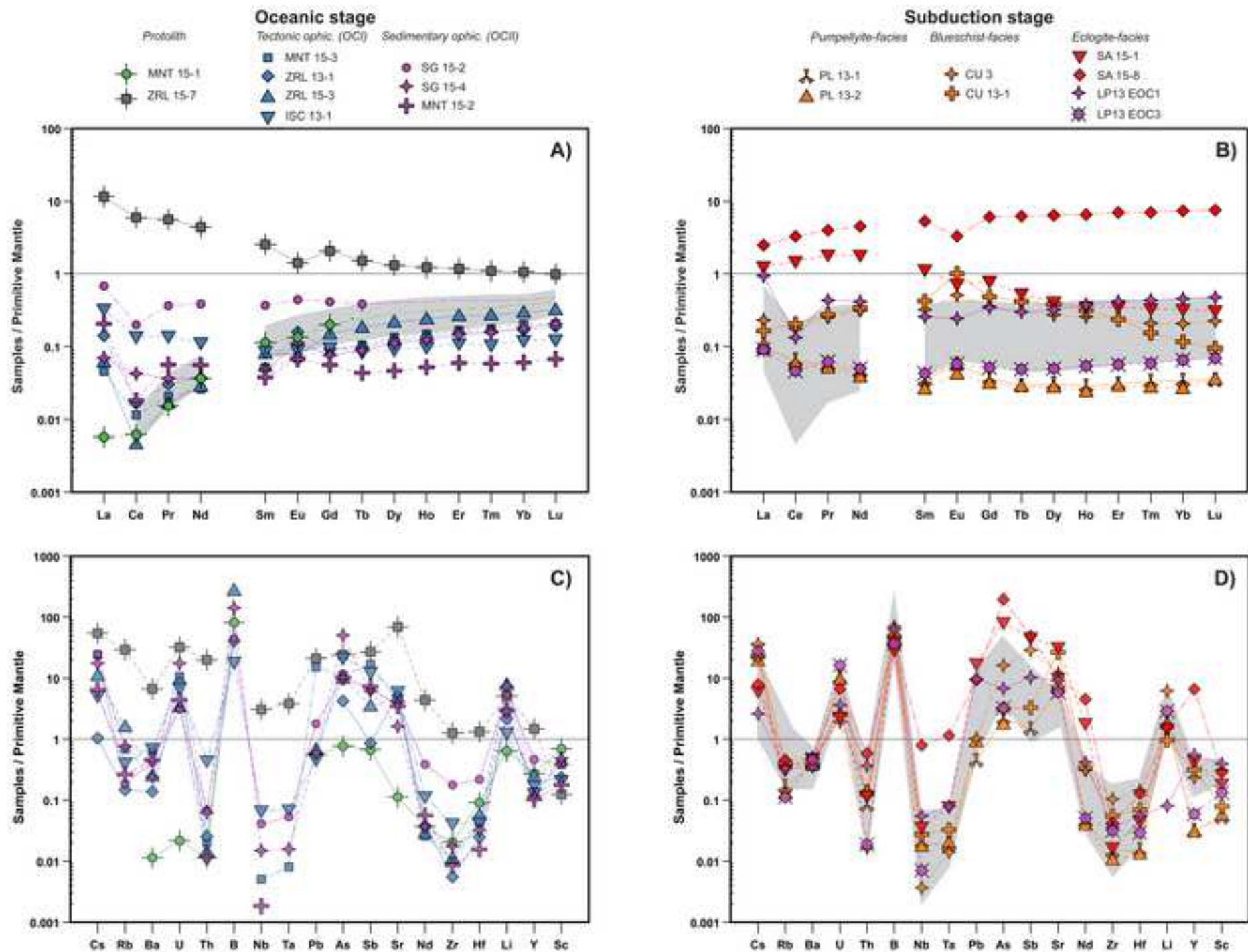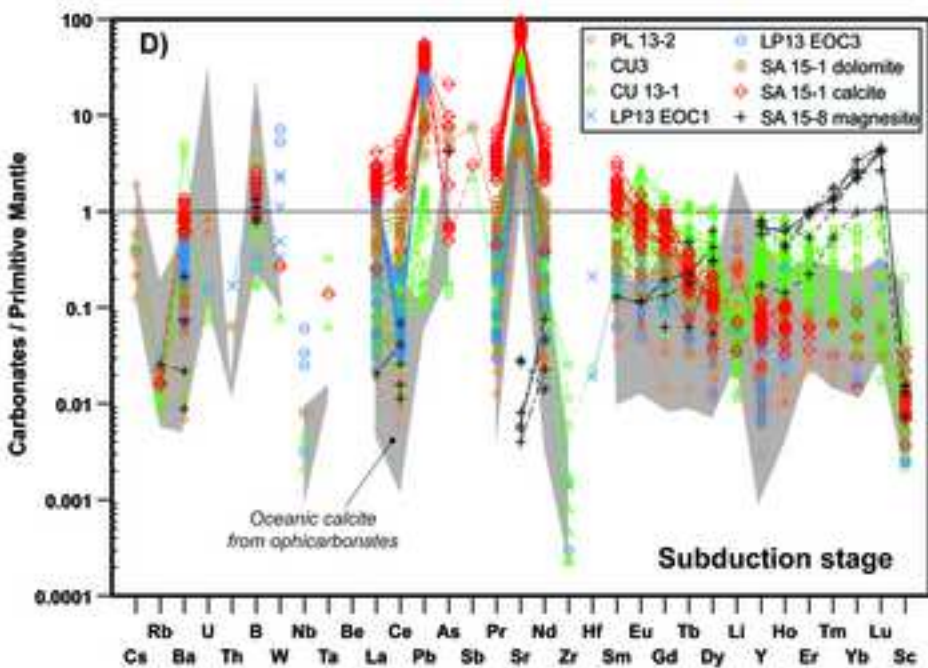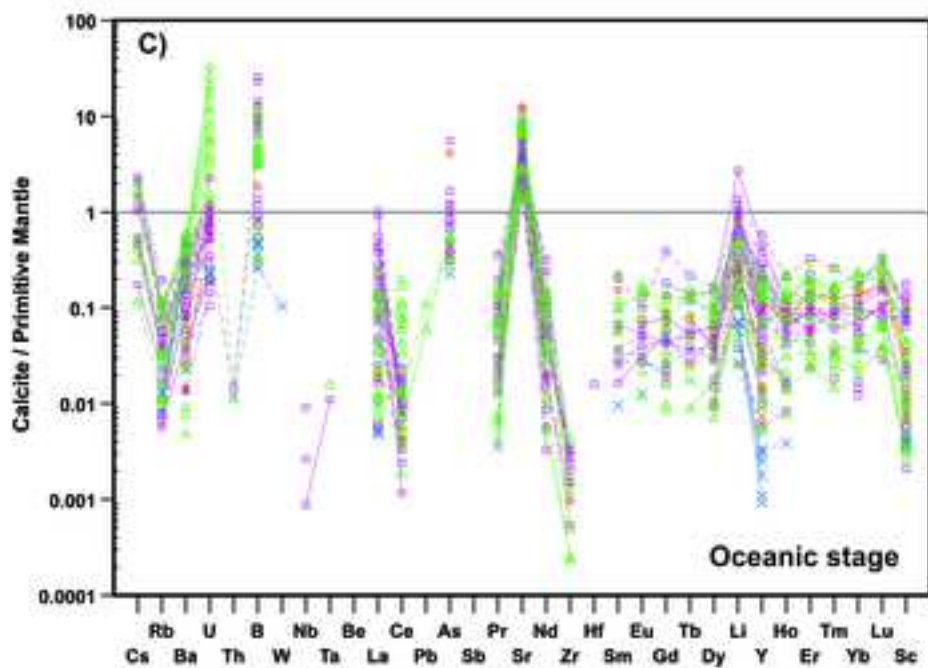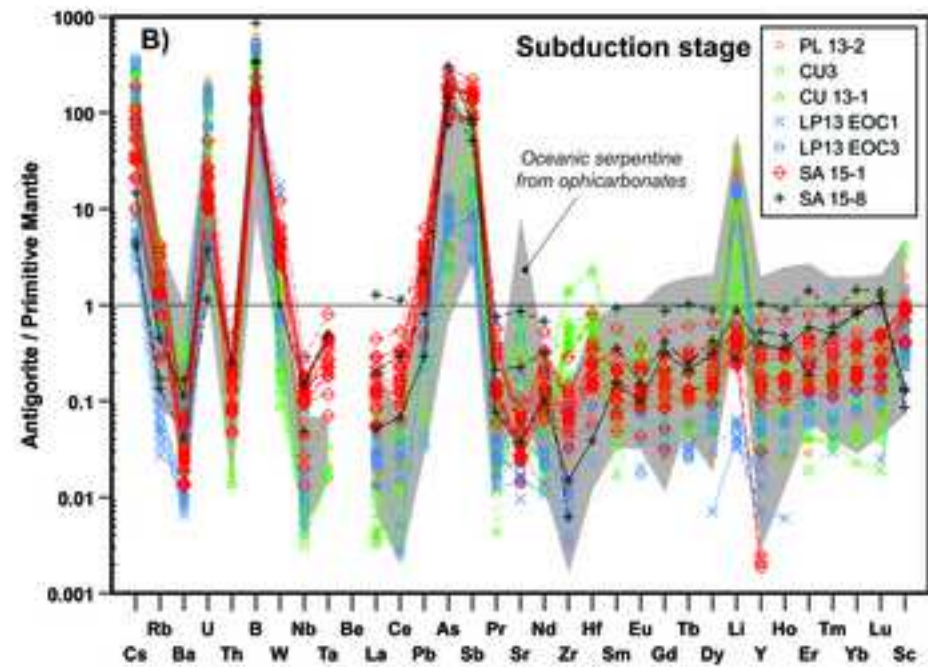**Click here to download high resolution image**
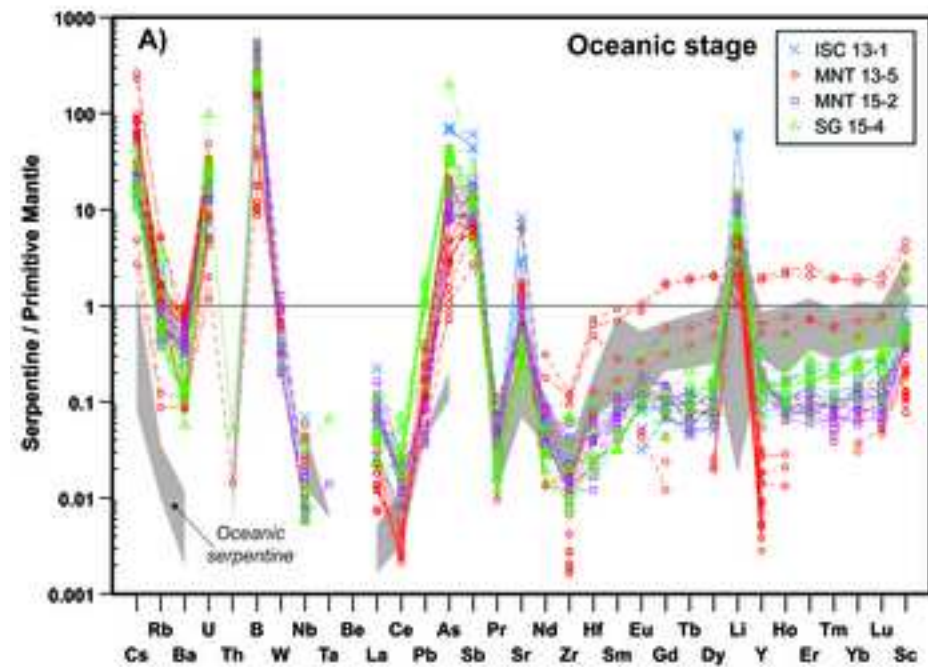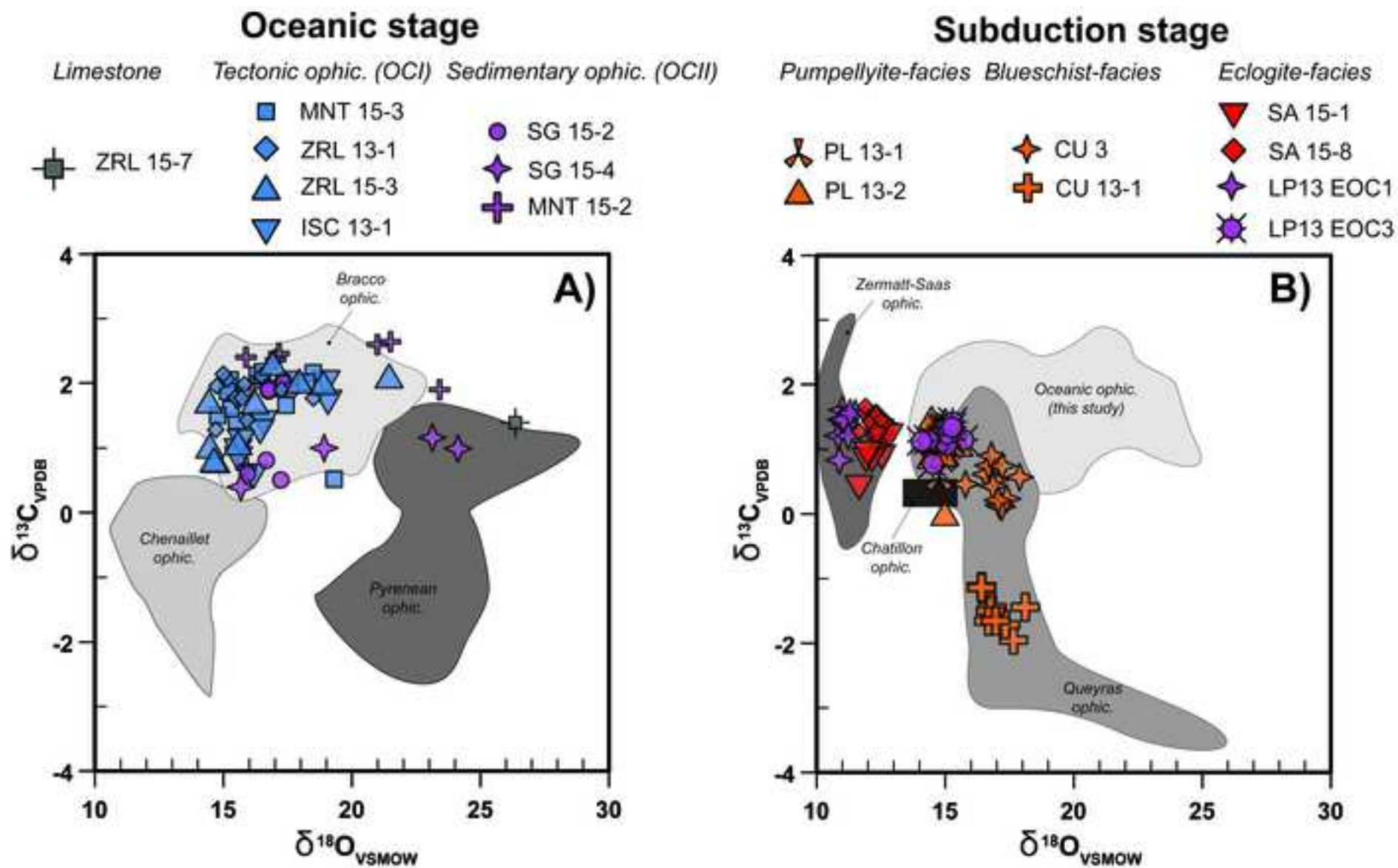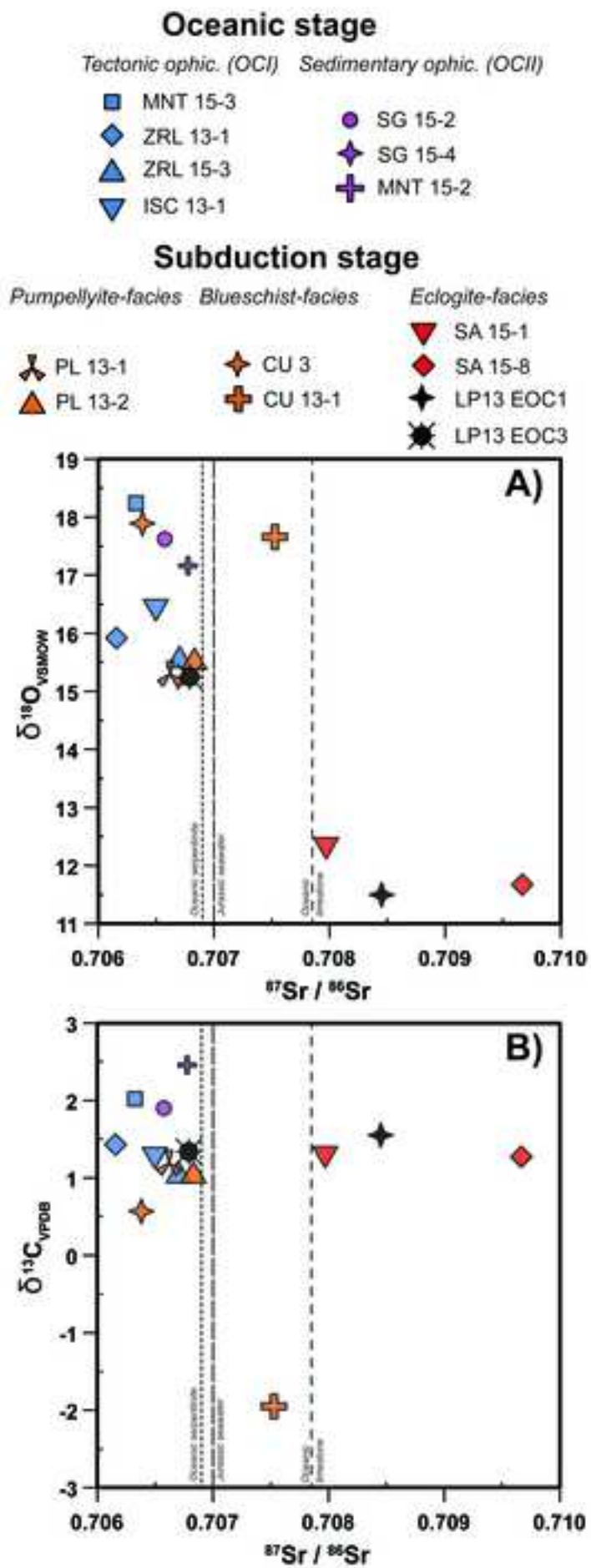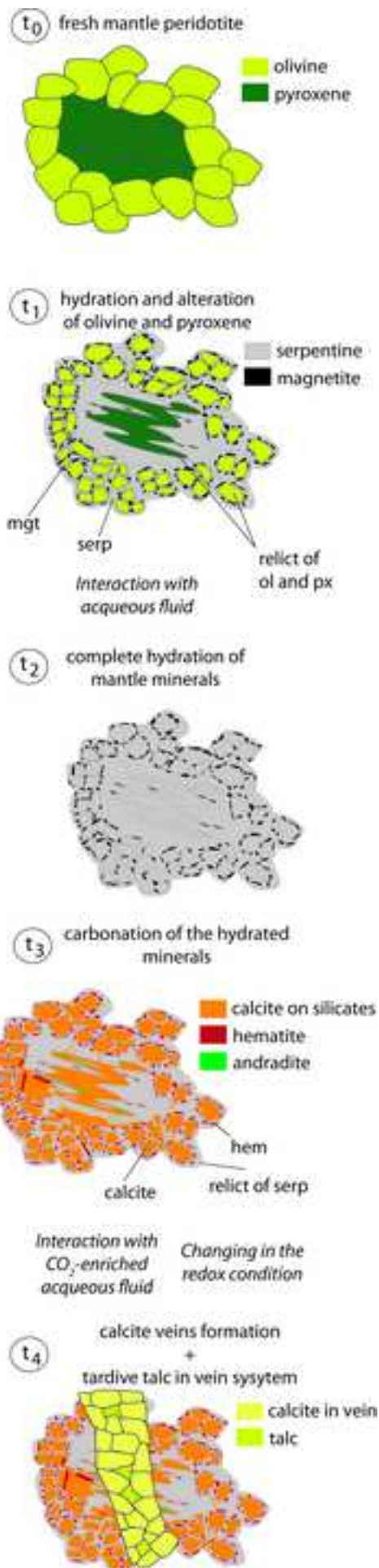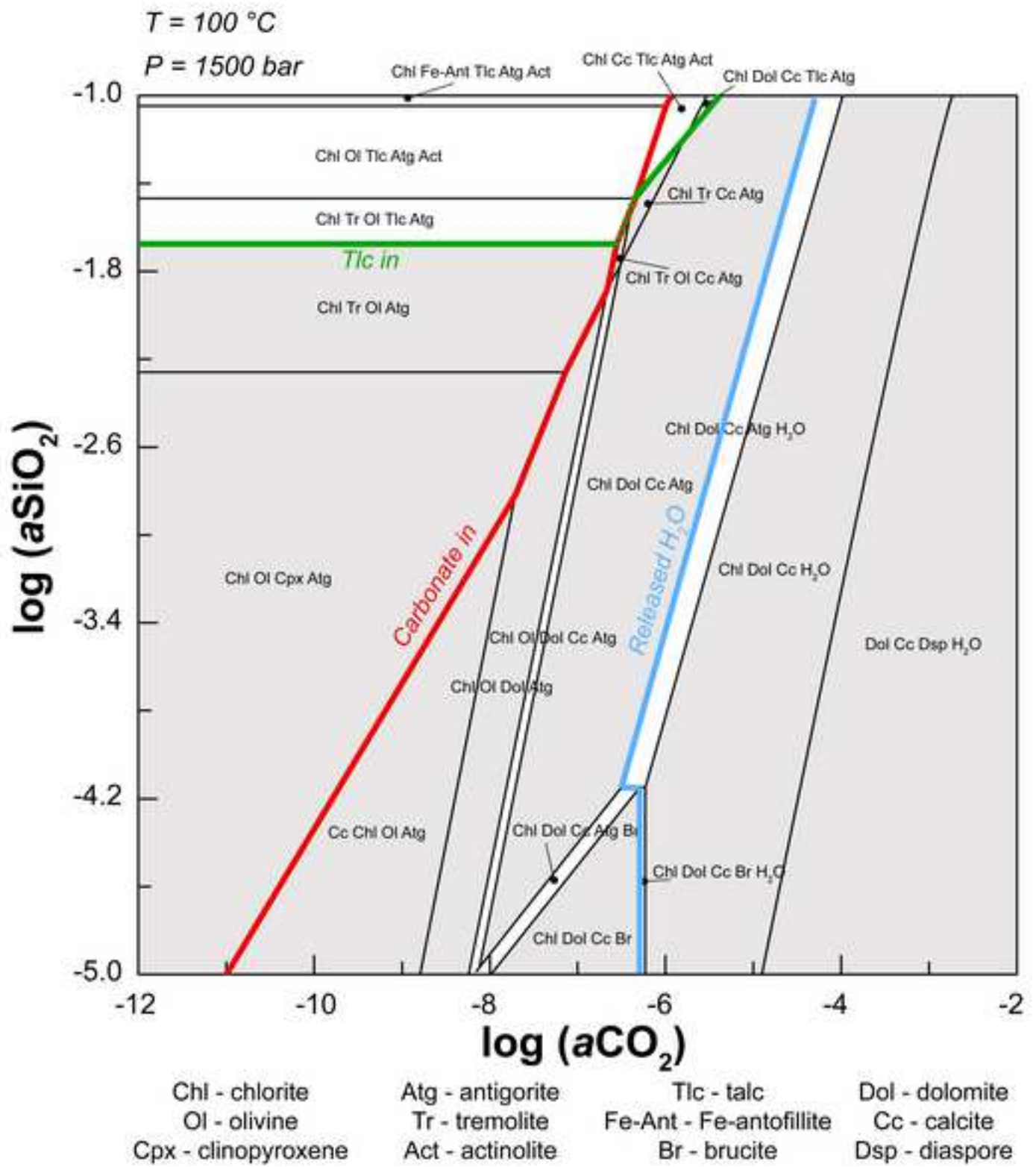
Figure 10

Figure 11
[Click here to download high resolution image](#)

Figure 11
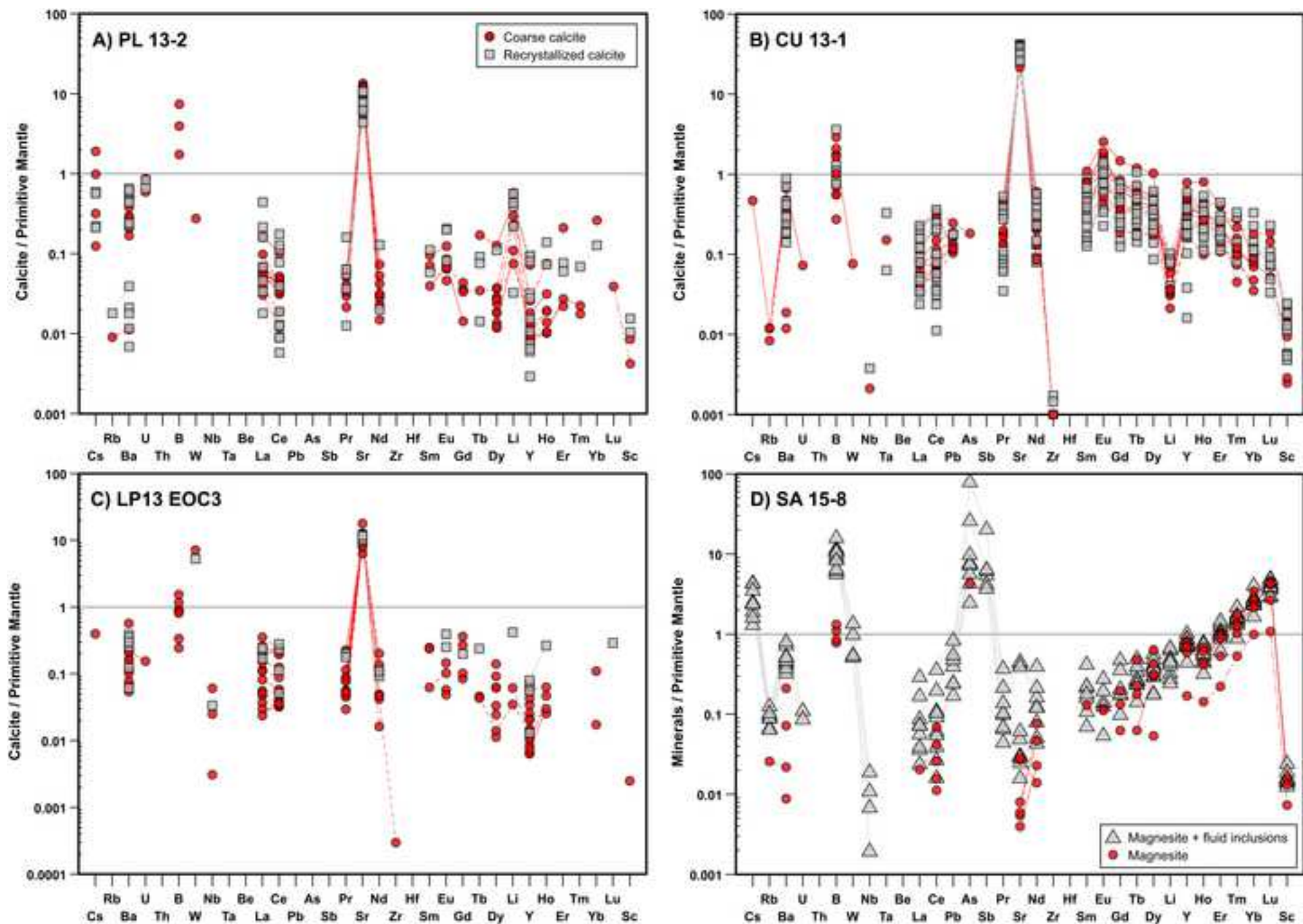
Table 1

Table 1. Whole-rock major (wt.%) and trace element (ppm) analyses for serpentinite, limestone and ophicarbonate rocks

	Oc. serp.	Limestone	Oc. tectonic ophicarbonates				Oc. Sedimentary ophicarbonates			Prograde ophicarbonates				Eclogite facies ophicarbonates			
	MNT 15-1	ZRL 15-7	MNT 13-5	ZRL 13-1	ZRL 15-3	ISC 13-1	SG 15-4	SG 15-2	MNT 15-2	PL 13-1	PL 13-2	CU 3	CU 13-1	SA 15-1	SA 15-8	LP13 EOC1	LP13 EOC3
GPS sample location	N 44.19811 E 9.58860	N 44.34558 E 9.45221	N 44.19811 E 9.58860	N 44.34558 E 9.45221	N 44.34558 E 9.45221	N 44.32808 E 9.44154	N 44.19654 E 9.58915	N 44.19654 E 9.58915	N 44.19811 E 9.58860	N 44.53202 E 88.181	N 44.53202 E 88.181	N 44.58542 E 6.92014	N 44.58542 E 6.92014	N 44.40907 E 8.54205	N 44.40907 E 8.54205	N 44.55364 E 8.44636	N 44.55364 E 8.44636
SiO_2	37.80	0.02	25.40	11.46	25.28	16.63	34.53	19.54	14.04	*Not determined*	6.96	21.22	6.13	13.05	18.66	21.26	12.59
Al_2O_3	1.69	0.01	1.09	0.65	1.57	1.27	1.10	1.71	0.54		0.16	1.14	0.24	0.25	1.34	1.03	0.52
$Fe_2O_3(Tot)$	8.37	0.03	5.14	3.43	5.92	5.56	6.53	5.26	3.17		1.20	3.28	1.59	2.92	8.47	4.97	2.67
MnO	0.123	0.080	0.071	0.080	0.098	0.093	0.124	0.092	0.100		0.042	0.124	0.114	0.121	0.413	0.063	0.056
MgO	37.14	0.17	15.75	10.29	21.34	10.45	31.57	14.38	12.90		6.16	14.71	4.81	14.41	25.82	19.58	11.51
CaO	0.12	57.73	26.35	39.95	20.77	34.91	8.42	30.52	35.96		46.51	31.46	47.96	34.57	16.28	26.28	38.67
Na_2O	<0.01	0.02	0.07	0.01	<0.01	0.03	<0.01	0.03	<0.01		<0.01	0.01	<0.01	<0.01	0.04	<0.01	<0.01
K_2O	<0.01	<0.01	<0.01	<0.01	0.02	<0.01	<0.01	<0.01	<0.01		<0.01	<0.01	<0.01	<0.01	0.01	<0.01	<0.01
TiO_2	0.045	0.020	0.026	0.013	0.030	0.013	0.023	0.051	0.007		0.003	0.036	0.013	0.008	0.043	0.019	0.007
P_2O_5	<0.01	<0.01	0.02	0.03	0.02	0.02	0.03	0.03	0.03		0.01	<0.01	<0.01	0.06	0.04	0.03	0.03
H_2O^*	13.32	<0.01	5.58	4.43	8.22	2.30	10.46	6.10	n.d.		3.51	4.71	0.92	7.70	15.44	6.36	2.75
CO_2	<0.01	41.88	19.50	30.00	16.50	28.00	7.00	22.30	n.d.		35.20	23.20	38.40	26.40	14.10	19.90	31.10
LOI	13.32	41.88	25.08	34.43	24.72	30.30	17.46	28.40	32.97		38.71	27.91	39.32	34.10	29.54	26.26	33.85
Total	98.61	58.12	99.01	100.30	99.79	99.28	99.79	100.00	99.73		99.75	99.90	100.20	99.49	100.70	99.50	99.89
Li	1.24	9.94	5.47	4.19	15.30	2.46	14.29	10.57	5.79	3.68	3.46	12.13	1.85	2.90	3.04	0.16	5.57
B*	24.6	22.6	n.d.	12.2	82.1	5.4	13.4	42.9	n.d.	17.4	16.2	21.1	10.9	8.6	12.8	18.9	10.9
Sc	14.9	2.22	7.13	4.41	8.42	3.89	9.39	7.38	3.26	0.97	1.06	5.81	1.43	3.30	5.36	7.22	2.44
V	57	18	32	24	48	30	41	22	16	5	5	29	6	12	30	30	12
Co	109.0	1.7	55.0	23.0	48.0	52.0	101.0	53.0	34.0	20.0	19.0	48.0	8.9	27.7	53.3	49.0	36.9
Ni	2200	13	1179	600	1015	1150	2000	880	870	350	350	790	160	430	500	950	750
Cu	44.0	26.0	39.0	39.0	45.0	12.2	17.0	25.0	23.0	100.0	13.6	22.9	15.5	21.7	22.0	90.4	17.8
Zn	62.00	33.00	28.00	33.00	35.00	32.17	31.70	40.00	23.00	49.00	13.69	23.94	14.77	18.46	43.59	40.53	17.08
Ga	1.443	2.795	0.974	0.604	1.204	0.862	1.119	1.219	0.428	0.096	0.106	0.841	0.215	0.389	2.759	0.974	0.296
As	0.038	1.202	0.551	0.212	0.500	1.072	2.504	0.504	0.515	0.109	0.087	0.803	0.155	4.071	9.737	0.339	0.162
Rb	b.d.l.	17.5	0.412	0.088	0.958	0.245	0.458	0.111	0.158	0.101	0.076	0.217	0.244	0.189	0.274	0.198	0.067
Sr	2.23	1365	86.1	103	97.1	120	32.1	74.3	68.9	137	155	236	525	633	212	184	117
Y	1.370	7.170	0.665	0.919	1.213	0.630	0.571	2.297	0.438	0.155	0.149	1.166	1.550	2.155	32.438	2.716	0.291
Zr	0.212	14.640	0.120	0.057	0.134	0.477	0.206	2.068	0.089	0.171	0.124	1.215	0.646	0.194	0.492	0.407	0.370
Nb	b.d.l.	2.410	0.008	b.d.l.	b.d.l.	0.056	0.012	0.036	0.001	0.020	0.018	0.007	0.026	0.032	0.621	0.047	0.009
Cd	0.034	0.447	0.101	0.245	0.099	0.227	0.090	0.180	0.160	0.072	0.072	0.184	0.043	0.168	0.139	0.073	0.060
Sb	0.004	0.148	0.092	0.005	0.019	0.068	0.034	0.035	0.040	0.008	b.d.l.	0.158	0.018	0.254	0.269	0.056	b.d.l.
Cs	b.d.l.	1.14	0.505	0.022	0.233	0.107	0.366	0.515	0.136	0.526	0.402	0.763	0.491	0.128	0.167	0.055	0.585
Ba	0.08	44.04	4.12	0.91	1.65	4.59	1.60	2.82	3.04	2.59	2.50	3.23	2.57	3.16	3.27	2.33	3.06
La	0.004	7.477	0.030	0.092	0.040	0.213	0.046	0.445	0.133	0.061	0.069	0.150	0.106	0.815	1.609	0.609	0.059
Ce	0.010	9.962	0.019	0.028	0.008	0.228	0.072	0.334	0.030	0.110	0.097	0.295	0.345	2.470	5.498	0.223	0.078
Pr	0.004	1.426	0.005	0.008	0.004	0.035	0.009	0.093	0.014	0.014	0.013	0.064	0.070	0.460	1.013	0.110	0.016
Nd	0.046	5.494	0.033	0.047	0.036	0.141	0.046	0.484	0.070	0.056	0.048	0.392	0.426	2.255	5.640	0.524	0.063
Sm	0.046	1.031	0.021	0.021	0.033	0.035	0.019	0.150	0.015	0.014	0.011	0.131	0.172	0.460	2.153	0.105	0.018
Eu	0.021	0.218	0.011	0.024	0.012	0.014	0.017	0.069	0.010	0.009	0.006	0.079	0.155	0.113	0.508	0.038	0.009
Gd	0.109	1.123	0.050	0.050	0.081	0.052	0.041	0.225	0.031	0.020	0.017	0.192	0.263	0.430	3.299	0.188	0.028
Tb	0.024	0.150	0.010	0.010	0.018	0.008	0.009	0.038	0.004	0.003	0.003	0.030	0.042	0.053	0.619	0.030	0.005
Dy	0.191	0.884	0.090	0.081	0.147	0.061	0.075	0.270	0.032	0.021	0.019	0.185	0.258	0.277	4.311	0.218	0.034
Ho	0.047	0.183	0.022	0.020	0.036	0.015	0.018	0.062	0.008	0.004	0.004	0.038	0.047	0.053	0.979	0.056	0.008
Er	0.146	0.516	0.074	0.068	0.117	0.048	0.064	0.191	0.026	0.014	0.013	0.104	0.104	0.153	3.077	0.184	0.025
Tm	0.024	0.075	0.012	0.011	0.019	0.007	0.011	0.029	0.004	0.002	0.002	0.014	0.010	0.023	0.476	0.030	0.004
Yb	0.168	0.469	0.090	0.074	0.130	0.053	0.080	0.194	0.027	0.015	0.012	0.092	0.051	0.144	3.267	0.202	0.029
Lu	0.028	0.067	0.014	0.013	0.022	0.008	0.014	0.032	0.005	0.002	0.002	0.015	0.006	0.021	0.513	0.032	0.005
Hf	0.026	0.371	0.012	0.007	0.016	0.012	0.009	0.062	0.004	0.004	0.004	0.040	0.020	0.013	0.036	0.016	0.008
Ta	b.d.l.	0.142	0.001	b.d.l.	b.d.l.	0.003	0.001	0.002	b.d.l.	0.001	0.001	0.001	0.001	0.003	0.042	0.003	b.d.l.
Pb	0.084	3.162	2.269	b.d.l.	0.101	0.069	0.089	0.267	b.d.l.	0.067	0.136	0.153	b.d.l.	2.602	1.410	1.457	b.d.l.
Th	0.001	1.567	0.002	0.002	0.001	0.035	0.005	0.005	0.001	0.007	0.011	0.001	0.011	0.009	0.046	0.029	0.001
U	0.001	0.740	0.242	0.197	0.077	0.158	0.400	0.071	0.101	0.234	0.221	0.044	0.059	0.052	0.154	0.083	0.368

*H_2O calculed as difference between LOI (loss of ignition) and CO_2 measured

n.d. - not determined

b.d.l. - below detection limits

* - data peformed at TIMS

Table 2. In situ major (in wt.%) and trace element (in ppm) composition of serpentine minerals

	MNT 15-1						MNT
	after pyroxene (n = 11)		after olivine (n = 8)		mesh (n = 3)		clast (n
		sd		sd		sd	
SiO$_2$	38.07	0.91	40.35	0.71	35.31	0.92	49.35
TiO$_2$	0.10	0.05	0.03	0.02	0.03	0.00	0.02
Al$_2$O$_3$	3.21	0.92	0.89	0.32	0.59	0.05	1.61
FeO	4.80	1.08	5.04	0.59	12.81	2.16	6.36
MnO	0.14	0.02	0.08	0.01	0.09	0.00	0.12
MgO	41.62	0.77	41.55	0.73	39.14	1.23	26.29
CaO	0.06	0.02	0.06	0.01	0.04	0.00	4.14
Na$_2$O	<0.01		<0.01		<0.01		0.11
K$_2$O	<0.01		<0.01		<0.01		0.60
Total	88.00		87.98		88.00		88.12
	n = 10		n = 8		n = 3		n =
Li	2.0	2.4	0.26	0.18	0.061	0.037	9.3
B	50	32	36	11	32	13	43
Sc	32	12	11	5	7.0	0.8	3.6
V	152	79	27	23	16	1	33
Cr	5900	2000	700	600	130	70	1200
Co	13	8	15	4	86	38	132
Ni	380	150	1600	400	2200	600	3100
Zn	12	5	9.2	1.5	8.8	1.0	34
As	0.008	0.002	<0.060		0.007	0.002	0.46
Rb	0.011	0.005	<0.023		0.008	0.001	0.97
Sr	2.5	1.4	2.2	0.5	1.8	0.1	22
Y	2.0	0.8	1.7	1.0	1.4	0.2	0.083
Zr	0.27	0.02	0.25	0.05	0.17	0.03	0.11
Nb	0.020	0.007	<0.017		<0.001		0.013
In	0.018	0.004	<0.014		0.006	0.001	0.012
Sb	<0.004		<0.072		<0.004		0.045
Cs	0.010	0.011	<0.019		0.002	0.000	1.5
Ba	0.032	0.024	<0.126		0.028	0.004	4.2
La	0.002	0.001	<0.013		0.001		0.012
Ce	0.012	0.004	<0.020		0.007	0.000	0.007
Pr	0.006	0.003	<0.011		0.003	0.000	0.005
Nd	0.082	0.028	0.12	0.03	0.052	0.005	0.079
Sm	0.078	0.038	0.21	0.07	0.053	0.012	0.13
Eu	0.036	0.018	<0.028		0.025	0.005	0.051
Gd	0.19	0.07	0.14	0.03	0.12	0.02	0.067
Tb	0.039	0.018	0.030	0.011	0.025	0.003	0.081
Dy	0.33	0.13	0.29	0.10	0.21	0.03	0.29

Table 3. In situ major (in wt.%) and trace element (in ppm) composition of carbonate minerals from

	MNT 13-5				ISC 13-1			
	clast (n = 14)		vein (n = 5)		clast (n = 28)		vein (n = 4)	
		sd		sd		sd		sd
SiO_2	<0.01		0.04	0.02	0.21	0.10	0.02	0.01
TiO_2	<0.01		<0.01		0.02	0.02	0.03	0.03
Al_2O_3	<0.01		<0.01		0.01	0.01	0.01	0.01
FeO	<0.01		<0.01		0.17	0.10	0.02	0.01
MnO	0.06	0.04	<0.01		0.20	0.12	0.10	0.09
MgO	0.02	0.01	0.54	0.22	0.51	0.35	0.31	0.18
CaO	54.87	2.54	54.42	0.61	56.02	3.58	56.41	1.74
Na_2O	0.01	0.01	<0.01		0.02	0.01	0.02	0.02
K_2O	<0.01		<0.01		<0.01		<0.01	
Total	54.96		55.00		57.15		56.91	
	n = 14		n = 5		n = 2		n = 7	
Li	0.75	0.47	0.39	0.02	0.094	0.030	0.45	0.09
B	0.48		0.55		0.14	0.05	0.93	0.05
Sc	0.44	0.33	0.30	0.21	0.069	0.008	1.6	0.1
V	0.44	0.34	0.20		0.009	0.005	0.82	0.40
Cr	6.6	2.8	2.7	1.9	1.9	0.2	11	6
Co	1.2	2.1	0.27	0.27	0.21	0.14	4.7	1.8
Ni	36	19	11	6	4.4	2.7	320	150
Zn	0.95	0.45	0.16	0.09	0.26	0.13	7.8	3.0
As	<0.014		0.083	0.108	0.021	0.010	0.092	
Rb	0.023	0.012	<0.007		0.006	0.002	0.024	0.008
Sr	89	26	160	80	120	50	120	10
Y	0.42	0.62	0.25	0.22	0.009	0.004	0.12	0.02
Zr	<0.008		0.010		<0.027		<0.001	
Nb	<0.005		<0.004		<0.003		<0.002	
In	<0.004		<0.003		<0.014		<0.014	
Sb	<0.020		<0.017		<0.075		<0.003	
Cs	<0.004		<0.004		0.026	0.011	0.026	0.011
Ba	0.36	0.18	0.39	0.35	1.5	1.1	1.2	0.3
La	0.014		0.012		0.004	0.002	0.019	
Ce	0.012	0.007	0.007		0.015	0.001	0.015	0.001
Pr	0.011		<0.003		0.001		<0.001	
Nd	0.056		0.025		<0.039		<0.014	
Sm	0.076	0.047	0.062		0.004		<0.018	
Eu	0.026		0.010		0.002		<0.003	
Gd	0.15	0.15	0.040		<0.037		<0.013	
Tb	0.053		0.008		<0.006		<0.001	
Dy	0.13	0.16	0.029	0.004	<0.020		<0.007	
Ho	0.045	0.048	0.013	0.003	0.001		<0.001	
Er	0.16	0.15	0.044	0.019	<0.023		<0.010	
Tm	0.047		0.007	0.001	<0.006		<0.001	

Table 4
Click here to download Table: Table_4_rev.xlsx

Table 4. Whole-rock C-O and Sr isotopic composition for serpentinite, limestone and ophicarbonate rocks

		$\delta^{18}O$ (‰)	$\delta^{13}C$ (‰)	Rb/Sr	$^{87}Sr/^{86}Sr$	err	*Jurassic age* $^{87}Sr/^{86}Sr_{160Ma}$	Δ (measured-160Ma)	*High-pressure age* $^{87}Sr/^{86}Sr_{33Ma}$	Δ (measured-33Ma)
Oc. serp.	**MNT 15-1**	*n.d.*	*n.d.*	-	0.706929	0.000038	0.706929	0.000000		
Limestone	**ZRL 15-7**	26.1	0.5	0.0128	0.707932	0.000009	0.707848	0.000084		
	MNT 13-5	10.9	1.4	0.0048	0.706355	0.000007	0.706323	0.000032		
OCI (tectonic	**ZRL 13-1**	15.7	0.6	0.0009	0.706162	0.000009	0.706156	0.000006		
ophic.)	**ZRL 15-3**	15.6	1.1	0.0099	0.706768	0.000016	0.706703	0.000065		
	ISC 13-1	16.2	0.4	0.0020	0.706510	0.000012	0.706497	0.000013		
OCII (sedimentary	**SG 15-4**	17.4	1.1	0.0143	0.705756	0.000009	0.705662	0.000094		
ophic.)	**SG 15-2**	15.9	-1.7	0.0015	0.706046	0.000022	0.706036	0.000010		
	MNT 15-2	17.0	1.6	0.0023	0.706790	0.000009	0.706775	0.000015		
	PL 13-1	15.1	0.3	0.0007	0.706624	0.000008	0.706619	0.000005		
Prograde	**PL 13-2**	15.3	0.2	0.0005	0.706833	0.000009	0.706830	0.000003		
ophicarbonates	**CU 3**	17.7	-0.3	0.0009	0.706383	0.000008	0.706377	0.000006		
	CU 13-1	17.1	-2.8	0.0005	0.707530	0.000009	0.707527	0.000003		
	SA 15-1$_{calcite}$	12.5	1.0	<0.0001	0.707969	0.000014	0.707969	0.000000	0.707969	0.000000
Eclogite facies	**SA 15-1**$_{dolomite}$	11.9	0.8	0.0001	0.708130	0.000022	0.708130	0.000000	0.708130	0.000000
ophicarbonates	**SA 15-8**	11.5	0.4	0.0013	0.709670	0.000009	0.709661	0.000009	0.709668	0.000002
	LP13 EOC1	11.3	0.7	0.0011	0.708453	0.000005	0.708446	0.000007	0.708452	0.000001
	LP13 EOC3	15.0	0.5	0.0006	0.706791	0.000010	0.706787	0.000004	0.706790	0.000001

n.d. - not determined

Supplementary Table A1

Supplementary Table A2

Supplementary Table A3

Appendix Figure A1

Supplementary material S1